Journal of Non-Newtonian Fluid Mechanics 261 (2018) 188–210

Contents lists available at ScienceDirect

Journal of Non-Newtonian Fluid Mechanics

journal homepage: www.elsevier.com/locate/jnnfm

Predictions for circular contraction-expansion flows with viscoelastoplastic & thixotropic fluids☆

J.E. López-Aguilar[a,b,*], M.F. Webster[b], H.R. Tamaddon-Jahromi[b], O. Manero[c]

[a] Facultad de Química, Departamento de Ingeniería Química, Universidad Nacional Autónoma de México (UNAM), Ciudad Universitaria, Coyoacán, CDMX 04510, Mexico

[b] Institute of Non-Newtonian Fluid Mechanics, Swansea University, Bay Campus, College of Engineering, Fabian Way, Swansea, SA1 8EN, United Kingdom

[c] Instituto de Investigaciones en Materiales, UNAM 04510, Mexico

ARTICLE INFO

Keywords:
Viscoelastoplasticity
Thixotropy
Micellar
Bautista–Manero/de Souza Mendes models
Enhanced-oil-recovery

ABSTRACT

In this predominately predictive modelling finite volume/element study, a comparative analysis is performed for *time-dependent* and *viscoelastoplastic* flow in a circular contraction-expansion geometry of aspect-ratio 10:1:10. For this, a hybrid finite volume/element scheme is employed. A new and revised micellar model is investigated, under the denomination of $BMP+\_\tau_p$, which reflects a bounded extensional viscosity response and an $N_{1\,Shear}$-upturn at large deformation rates (lost in earlier model-variants), a versatile model capable of supporting plasticity, shear-thinning, strain softening-hardening and shear-banding. Many of these features are common to wormlike micellar and polymer solutions. Then, findings are contrasted against a *de Souza Mendes* model. Two flow regimes are addressed: *plastic flow* (low flow-rate $Q \leq 1$ units, solvent-fraction $\beta < 10^{-1}$) and *viscoelastic flow* (larger-$Q > 1$; minimised plasticity; $\beta = 1/9$); as quantified via *flow-structure, yield-fronts and pressure-drops*. Under the *plastic regime*, elasticity-increase causes asymmetry about the contraction-plane, whilst yield-stress and enhanced strain-hardening promote solid-like features, apparent through augmented unyielded-regions and rising pressure-drops. Concerning the *viscoelastic regime* and vortex-structures, extensional-deformation experienced correlates with hardening expectation in uniaxial-extension, whilst streamline activity in vortex-cells correlates with normal-stress response in shear. Adjustment in strain-hardening/softening response with *Q-rise*, provides translation from *weaker* salient-corner vortex centres to *stronger* elastic corner-vortices; yet, when softening finally prevails, asymmetric upstream/downstream salient-corners vortex patterns are recovered. For strong-hardening and solvent-dominated $\beta \sim 0.8$ fluids (as with *Boger fluids*), an intermediate *lip-vortex-formation* phase is noted, alongside coexistence of salient-corner vortices. Such a vortex-coexistence phase is distinctly absent in solute-concentrated fluids.

1. Introduction

The *theme of this predictive study* is that of thixotropic-viscoelastoplastic flow in complex deformation. The constitutive equations employed reflect this and are model variants from the classes of Bautista–Manero [1–8] and de Souza Mendes [9–11]. The study is conducted under a flow-rate *(Q)*-increase protocol, and hence, under fixed fluid relaxation-time (Maxwellian averaged, λ_1). Such a procedure mimics the experimental set up, for which generally, a test fluid is pumped through an apparatus at a fixed steady-state flow-rate (*Q*), whereupon increase in flow-rate is initiated in incremental steps between steady-states. Under such prevailing steady-state conditions, and/or during transients between steady-states, relevant measurements may be performed to account for - (i) the influence of fluid-characteristics on flow-structure (streamlines from particle velocimetry, stress-fields from flow birefringence), and (ii) the forces required to maintain these flow conditions (pressure-drops in contraction/contraction-expansions; drags in flow past objects). Bearing this in mind, the present analysis aims to numerically predict the flow of such fluids through a circular sharp-cornered contraction-expansion of aspect-ratio $\alpha = 10$. This particular choice of geometry and contraction-ratio, exhibits many and varied features observed experimentally for some Boger fluids [12], that have been reproduced recently by continuum modelling using the swanINNFM(q) model [13]. There, complex vortex-phasing was retrieved, in which co-existence of lip and salient-corner vortices at intermediate flow-rates, evolved into strong elastic-corner vortices at high flow-rates. This was accompanied by adjustment in excess pressure-drop levels by some ~600%. Accordingly, with the potential of this flow-geometry to

☆ Dedicated to the memory of our dear colleague and friend, late Professor Mike Webster.

* Corresponding author at: Facultad de Química, Departamento de Ingeniería Química, Universidad Nacional Autónoma de México (UNAM), Ciudad Universitaria, Coyoacán, CDMX 04510, Mexico.

E-mail address: jelopezaguilar@unam.mx (J.E. López-Aguilar).

https://doi.org/10.1016/j.jnnfm.2018.09.001
Received 18 January 2018; Received in revised form 4 September 2018; Accepted 5 September 2018
Available online 6 September 2018
0377-0257/

Acronyms and abbreviations

a	dSM model kinetic parameter
ABS-f	ABSolute *f*-functional correction
b	dSM model kinetic parameter
BMP	Original Bautista–Manero–Puig model variant, see [1]
BMP+_τ_p	Latest Bautista–Manero–Puig model variant; see present work & [38]
dSM	de Souza Mendes model, see [7,9–11]
$\boldsymbol{D}$	Rate-of-deformation tensor
ecv	Elastic-corner vortex
epd	Excess pressure-drop
f	Structural *f*-functional
FENE	Finite Extensible Non-linear Elastic models
$G_s(\lambda)$	Structure-dependent elastic modulus, dSM model
G_0	Elastic modulus at vanishing shear-rates
IKH	Isotropic-Kinematic Hardening model
IVP	Initial-value-problem
II_{τ_p}	Second-invariant of the polymeric stress tensor
II_D	Second-invariant of the rate-of-deformation tensor
K	Power-law consistency coefficient
k_0	Inverse of the structure-destruction stress
KEP	Kinetic Elasto-Plastic model
LAOS	Large Amplitude Oscillatory Shear
L	Characteristic length
lv	Lip-vortex
m	dSM model kinetic parameter
MH	Moderate-Hardening fluid
n	Power-law index
N_1	First normal-stress difference in complex flow
N_{1Shear}	First normal-stress difference in simple shear flow
NH	No-Hardening fluid
NM_T	New Micellar total-stress-based model, see [4]
NM_τ_p	New Micellar polymeric-stress-based model, see [4]
p	Isotropic pressure
PTT	Phan-Thien-Tanner models
Q	Flow-rate
Re	Non-dimensional group Reynolds number
sc	Salient-corner vortex
SH fluid	Strong-Hardening fluid
SGR model	Soft Glassy Rheology Model
STZ model	Shear Transformation Zone model
swanINNFM(q)	Swansea-Institute of Non-Newtonian Fluid Mechanics model, see [13]
$\boldsymbol{T}$	Total stress tensor
T_{rz}	Shear-stress
t	Time
t_{eq}	Characteristic-time for structure-equilibrium, dSM models
$\boldsymbol{u}$	Velocity
U	Characteristic velocity
VGR	Velocity-Gradient Recovery correction
Wi	Non-dimensional group Weissenberg number

Greek symbols

α	Contraction-expansion of aspect-ratio
β	Solvent-fraction
Δp_{total}	Total pressure-drop
$\dot{\gamma}_{0d}$	Shear-rate level for transition between τ_0 to τ_{0d}, dSM model
η_{Ext}	Uniaxial extensional viscosity
η_p	Polymeric viscosity
η_{p0}	Polymeric viscosity at zero shear-rates
η_s	Solvent viscosity
η_{ss}	Steady-state polymeric viscosity, dSM model
∇	Gradient operator
λ^m	dSM structure-parameter
λ_{ss}	Steady-state dSM structure-parameter
λ_1	Relaxation time
$\lambda_1\dot{\gamma}$	Non-dimensional shear-rate
λ_s	Characteristic time of structure construction, Bautista–Manero models
ω	Non-dimensional structural construction parameter, Bautista–Manero models
ω_{DS}	Non-dimensional structural construction parameter, dSM models
ρ	Fluid density
$\boldsymbol{\tau}_p$	Polymeric stress tensor
τ_0	Dynamic yield-stress parameter, dSM model
τ_{0d}	Static yield-stress parameters, dSM model
ξ	Non-dimensional viscous-structural destruction parameter, Bautista–Manero models
ξ_{G_0}	Non-dimensional elastic-structural destruction parameter, Bautista–Manero models
Ψ_{sal}	Vortex intensity
Ψ_{sal_avg}	Average vortex intensity

reveal such strong and complex features of flow-structure and energy exchange, two flow regimes are selected here for further analysis: a *viscoelastic regime* and a *plastic regime*. The *viscoelastic flow regime* applies at intermediate-to-high flow-rates, in which purely-liquefied viscoelastoplastic material flows, where flow-structure is tracked via vortex dynamics and first normal-stress difference. The *plastic flow regime* occurs at low flow-rates, in which some solid-like features also arise, and which are evaluated, in flow-structure, through yield-fronts, and, in energetic aspects, through pressure drops. Then under complex deformation, the prevalent rheological properties to study, include shear-thinning, strain-hardening/softening, thixotropy and plasticity.

Viscoelastoplastic materials and their application Viscoelastoplastic materials are ubiquitous in the man-produced goods (paints, cements, foams, tooth paste, mayonnaise, waxy oils, foodstuff) and fluids in nature (blood, sputum, tissues) [14,15]. Particular attention has been devoted to oil-extraction, drilling muds and transport of waxy oils in pipe-lines [14–16]. Recent studies point out the necessity of a viscoelastic contribution in characterising previously-considered simple yield-stress materials as Carbopol in particle-settling and other complex flows, where a combination of shear and extensional deformations promote viscoelastoplastic and thixotropic response [17–20], and for which novel measurements of extensionally-active features are of importance [21]. Moreover, plastic-to-liquid like transition has been considered as a consequence of a dynamic structure-destruction and reformation, hence, introducing a thixotropic ingredient to explain such a response [15,22]. This recent interest in the time-dependent side of the yielding phenomenon is reflected in an increasing number of publications considering thixotropy and viscoelasticity to approximate the response of viscoelastoplastic materials in ideal and complex flows [23], fact that stands as a motivation from the present and previous works [6,7].

On constitutive modelling Typical and representative constitutive equations for these thixotropic and viscoelastoplastic fluids are constructed upon coupled stress and fluid-structure equations. Bautista–Manero model fluids were originally proposed to approximate the rheology of wormlike micellar solutions [1–5,8]. That is, so-called *'smart fluids - viscoelastic surfactants',* given their ability to break and reform their internal structure, subject to the changing environmental conditions of deformation they are exposed to. As such, they are useful to provide versatility - as injectant fluids in enhanced oil-recovery, drag-reducing agents, thickeners in personal products (shampoos, body soaps) and household products (hard-surface cleaners, drain-openers, liquid dishwashing detergents), and carriers in drug-delivery systems [24,25]. In contrast, de Souza Mendes model variants were devised to represent the rheology of crude-oils and waxes [9–11,26]. Despite their disparate origin, these two models have in common an additional partial differential equation, to describe the dynamic evolution of fluid-structure, enacted through mechanisms of construction and destruction. Within the oil-rheology-based constitutive models, one may find equations-of-state that combine a descriptive framework of viscoelasticity, through a fluid-structure description, and plasticity, through a Bingham-type yield-stress response. Examples are the Isotropic-Kinematic Hardening model (IKH model; [27]) and models that merge the plastic Bingham-like and viscoelastic Oldroyd-B-like fluid response [28,29]. There is an alternative point of view to model viscoelastoplastic materials based on the description of their microstructure; such models aim to describe the physical interactions between constituents of these materials at the microscale and, then, retrieve macroscale predictions of rheological properties. Illustration of such models are the *Soft Glassy Rheology* SGR-model [30,31], which apart from predicting yield-stress features, it models shear-banding under LAOS [32,33]; the Kinetic Elasto-Plastic KEP-model [34] and the Shear Transformation Zone STZ-model [35].

With both Bautista–Manero and de Souza Mendes models, such a set of constitutive equations reflects distinct properties of shear-thinning, strain-softening/hardening, first normal-stress difference, yield-stress and shear-banding [36–38]. The first normal-stress difference response in shear-deformation N_{1Shear} is highly non-linear, with a second upturn at high shear-rates. Nevertheless, some essential differences between the models are apparent: (i) through the *nature of the structure parameter* - the Bautista–Manero structure-parameter represents a dimensionless fluidity $f = \frac{\eta_{p0}}{\eta_p}$, whilst the de Souza Mendes structure-parameter reflects a dimensionless elastic modulus $\lambda^m = \frac{G_0}{G_s(\lambda)}$; (ii) this difference in structure-parameter interpretation provokes adjustment to the *polymeric extra-stress equation* - Bautista–Manero fluids fit well into an Oldroyd-B-type stress-equation, in which the structure-parameter only affects the source stress-term (i.e. $f\boldsymbol{\tau}_p$); alternatively, de Souza Mendes fluids somewhat alter such traditional differential-form, with the structure parameter modulating both the source stress-term and the non-linear upper-convective derivative stress-term (i.e. $\overset{\nabla}{\boldsymbol{\tau}}_p$); (iii) within the structure-destruction term of the structure-parameter equation, the *factor driving the non-linear evolution features* differs – this being the dissipation-function for Bautista–Manero models; whilst correspondingly, de Souza Mendes model early variants contain a dimensionless stress-tensor second-invariant [9,10] (latterly replaced by unity in a corrected de Souza Mendes version [11]); (iv) *elasticity in the structure equation*: whilst some Bautista–Manero model variants have an explicit contribution from the fluid relaxation-time λ_1 in the destruction-term [4–8], de Souza Mendes forms are devoid of this [9–11]. Naturally, such similarities and differences motivate the present investigation.

Enhancing numerical tractability - ABS-f- and VGR-corrections – Non-ideal yield-stress materials, such as heavy oil-fractions, suspensions and pastes, may be represented as extremely solute-concentrated (solvent-fractions of $\beta \leq 10^{-1}$) viscoelastic fluids. These high levels of polymer-concentration (>90%), together with the high deformation-rates imposed by the increase-flow-rate protocol adopted, pose considerable challenge to effective predictive modelling in retaining numerical tractability. This is so, even at modest levels of viscoelasticity. As such, enhanced numerical stability is afforded through a Velocity-Gradient Recovery correction (*VGR*-correction) and the ABSolute *f*-functional correction (*ABS-f*-correction). In this, *VGR*-correction imposes shear-free extensional deformation along the symmetry-line and a discrete correction for continuity; whilst ABS-*f*-correction to the constitutive-model structure-functional *f*, guarantees thermodynamic consistency and ensures positive viscosity estimation in complex flow (see [5]). These corrections are devised to constrain the loss of *initial-value-problem* (*IVP*) evolution and its consequent lack of positive definiteness in the system, alongside error propagation (see [5,8] and Section 3 below). Such corrections have been implemented successfully in a number of applications, as exemplified through the simulation of - wormlike micellar fluids in complex flow in non-banding [5,8] and banding conditions [38], the flow of viscoelastoplastic fluids in contraction-expansions (rounded-corner, $\alpha = 4$; [6,7]), and the flow of Boger fluids in contraction-type flows. The work on Boger fluids has resulted in the close match of some well-founded experimental pressure-drop data (also flow-structure), encompassing contraction-expansion and contraction forms, planar/circular configurations [39], rounded/abrupt corners [13,39–41], hyperbolic shape [42–44], and change in contraction-ratio [13].

2. Governing equations, constitutive modelling & theoretical framework

The relevant field equations for the flow problem in hand are those governing mass conservation and momentum transport, coupled to an equation-of-state for stress. Taken in non-dimensional form, the mass and momentum equations may be expressed, under incompressible and isothermal conditions, as:

$$\nabla \cdot \boldsymbol{u} = 0, \tag{1}$$

$$\mathrm{Re}\frac{\partial \boldsymbol{u}}{\partial t} = \nabla \cdot \boldsymbol{T} - Re\boldsymbol{u} \cdot \nabla \boldsymbol{u} - \nabla p. \tag{2}$$

Here, t represents time, spatial-gradient and divergence differential operators apply over the problem domain, with field variables $\boldsymbol{u}$, p and $\boldsymbol{T}$ of fluid-velocity, hydrodynamic-pressure and total viscoelastic-stress contributions, respectively. Then, the total viscoelastic-stress ($\boldsymbol{T}$) may be segregated into two parts: a solvent-component $\boldsymbol{\tau}_s$ (viscous-inelastic$\boldsymbol{\tau}_s = 2\beta\boldsymbol{D}$), and a polymeric nonlinear-component $\boldsymbol{\tau}_p$. Though plasticity may be introduced into either solvent or polymeric components, or indeed both, here the theme is to consider only contributions arising from those of a polymeric source. Hence, the viscoelastoplastic nature is embedded in a unified form through the networked structure of the material in a combined manner.

Adopting $\boldsymbol{D} = (\nabla \boldsymbol{u} + \nabla \boldsymbol{u}^{\mathrm{T}})/2$ is the rate-of-deformation tensor, for which superscript '$^{\mathrm{T}}$' denotes tensor-transpose operation, then dimensionless variables may be established as:

$$\boldsymbol{x}^* = \frac{\boldsymbol{x}}{L}, \quad \boldsymbol{u}^* = \frac{\boldsymbol{u}}{U}, \quad t^* = \frac{U}{L}t \quad \boldsymbol{D}^* = \frac{L}{U}\boldsymbol{D},$$

$$\boldsymbol{\tau}_p{}^* = \frac{\boldsymbol{\tau}_p}{(\eta_{p0} + \eta_s)\frac{U}{L}}, \quad p^* = \frac{p}{(\eta_{p0} + \eta_s)\frac{U}{L}}.$$

This provides for a reference zero shear-rate total viscosity, $(\eta_{p0} + \eta_s)$, in the viscoelastic regime, with zero-rate polymeric-viscosity η_{p0}, and η_s the constant solvent-viscosity. Based upon these definitions, a solvent-fraction $\beta = \eta_s/(\eta_{p0} + \eta_s)$ may be adopted, extracting the non-dimensional group Reynolds number $\mathrm{Re} = \rho U L/(\eta_{p0} + \eta_s)$. Parameters are then: material density ρ, and characteristic scales of U on velocity (mean velocity, based on volume flow-rate) and L on spatial-dimension (based on minimum contraction-gap dimension). Hence, a natural rate-scale to adopt emerges as (U/L).

The degree of elasticity is interpreted through the non-dimensional group Weissenberg number, $Wi = \lambda_1 U/L$, defined on the product of a

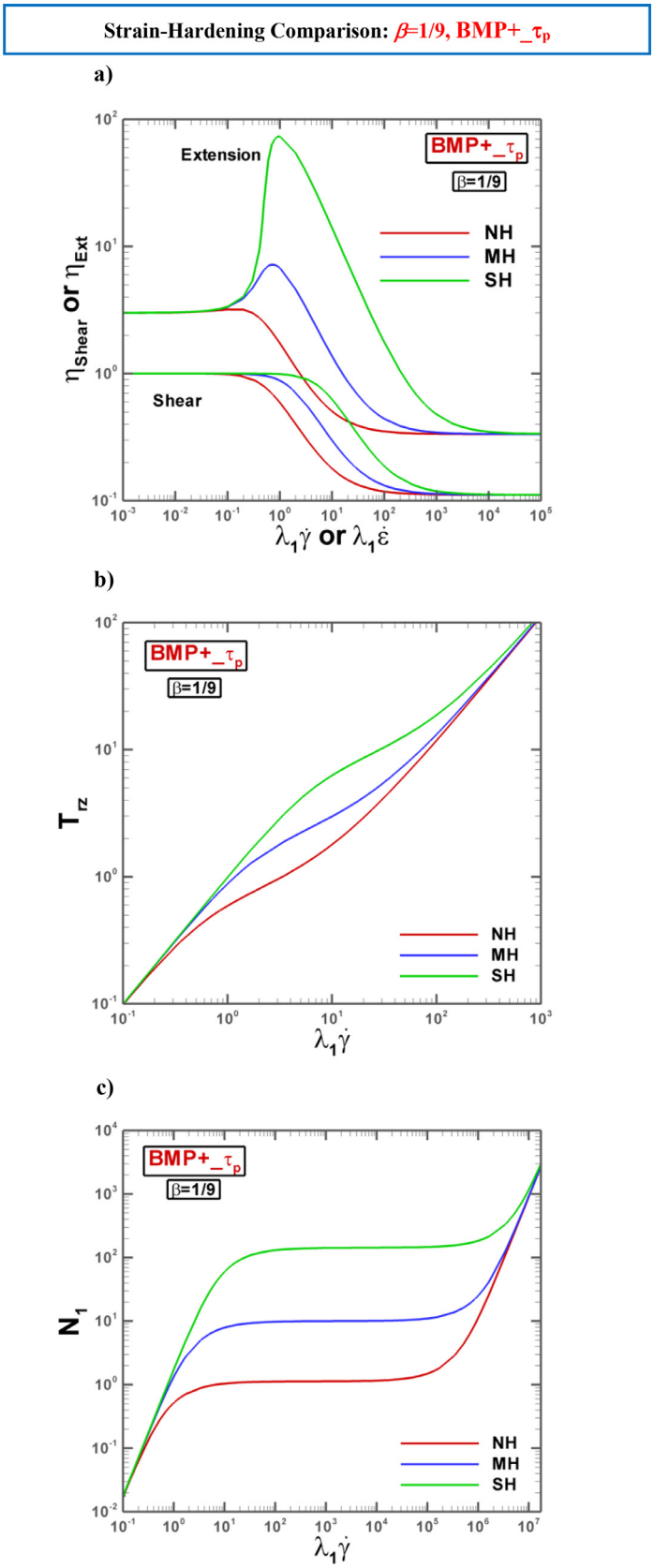

Fig. 1. a) η_{Shear} and η_{Ext}, b) T_{rz} and c) N_{1Shear}; BMP+_τ_p; $\beta = 1/9$; hardening comparison: NH $\{\omega, \xi_{G0}\} = \{4, 1\}$, MH $\{\omega, \xi_{G0}\} = \{4, 0.1125\}$, SH $\{\omega, \xi_{G0}\} = \{0.28, 0.1125\}$.

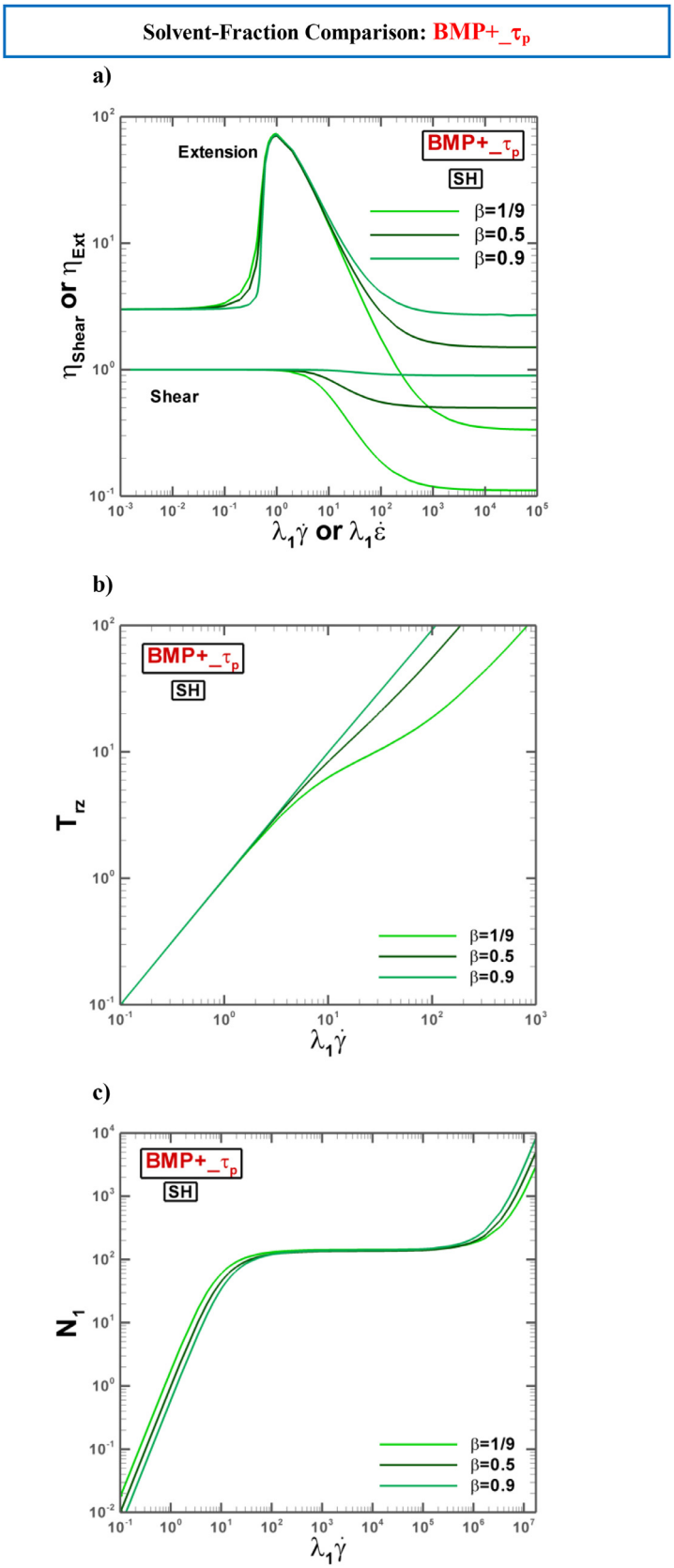

Fig. 2. a) η_{Shear} and η_{Ext}, b) T_{rz} and c) N_{1Shear}; BMP+_τ_p; SH fluids solvent-fraction comparison: $\beta = \{0.9, 0.5, 1/9\}$.

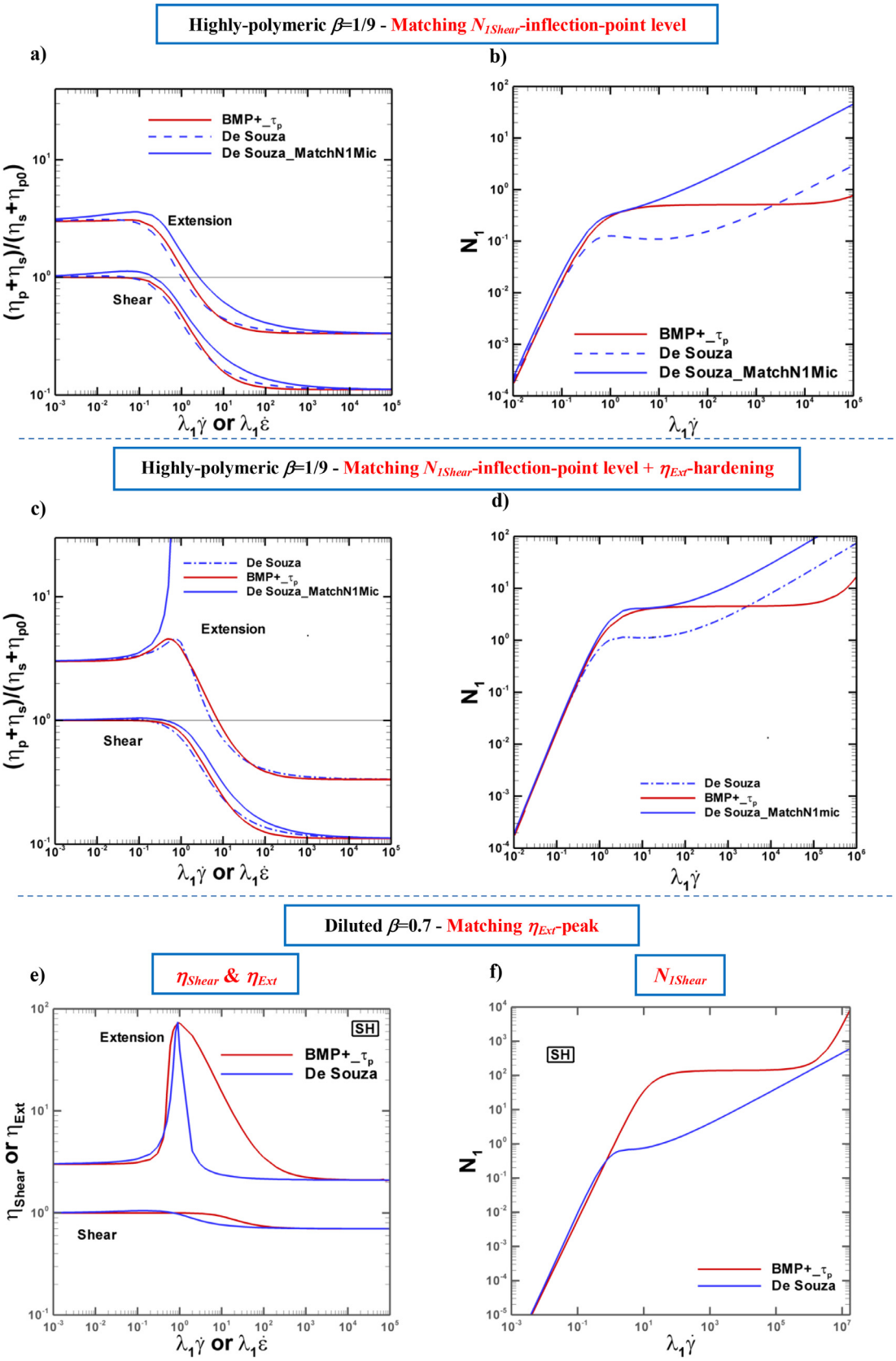

Fig. 3. Material functions: BMP+_τ_p v dSM (a-b) NH fluids, $\beta = 1/9$, N_{1Shear}-inflection-point matching across models; (c-d) MH fluids, $\beta = 1/9$; N_{1Shear}-inflection-point matching across models + hardening; (e–f) SH fluids, $\beta = 0.7$, η_{Ext}-peak matching across models.

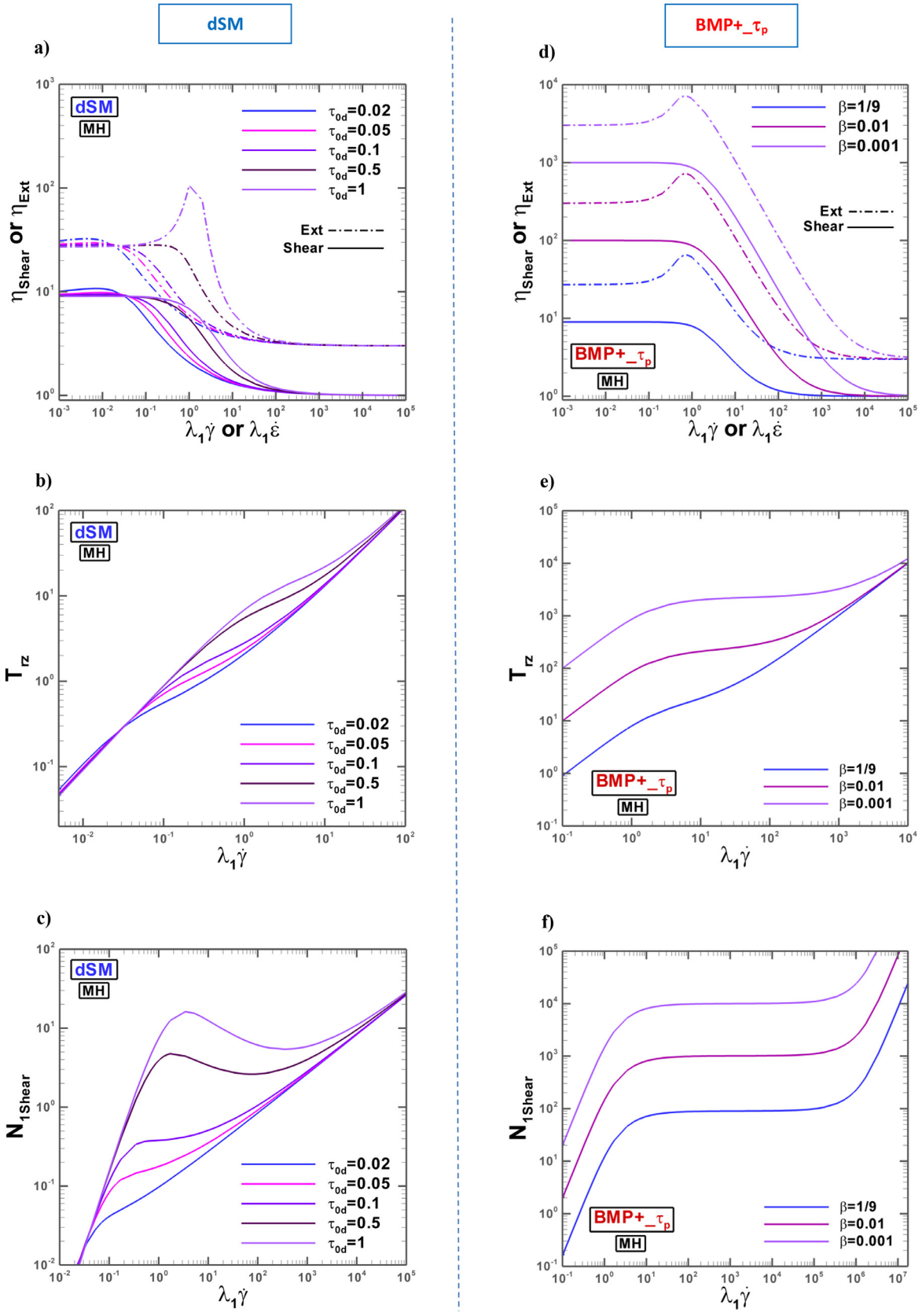

Fig. 4. η_{Shear} and η_{Ext}, T_{rz} and $N_{1\,Shear}$; dSM (left) and BMP+_τ_p (right); second Newtonian-plateau scaling; MH fluids.

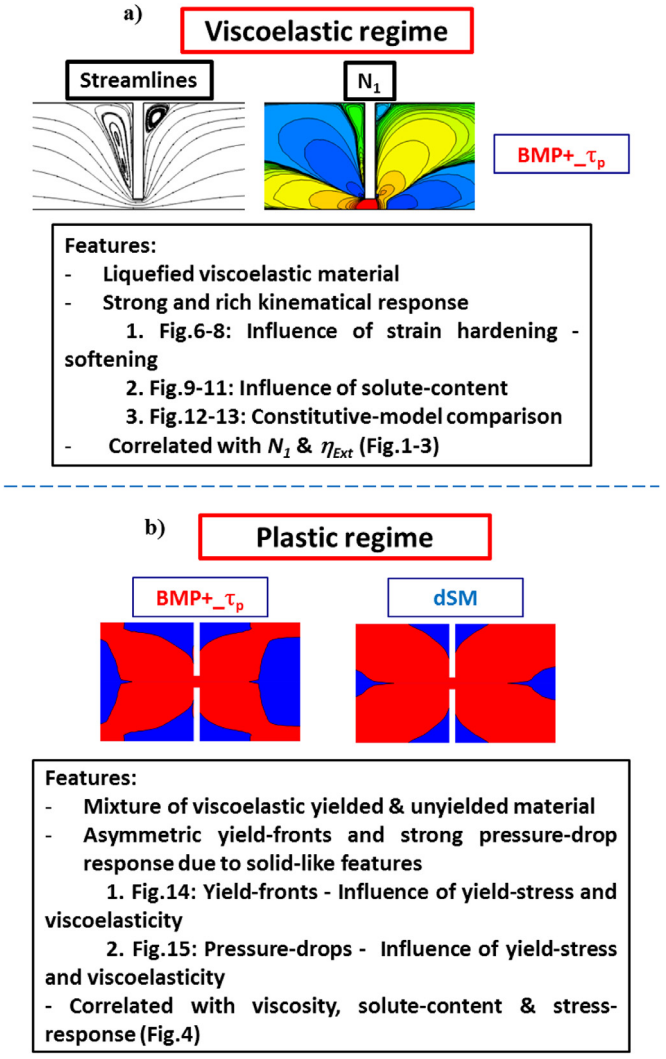

Fig. 5. Results section outline; a) viscoelastic regime; b) plastic regime.

characteristic material relaxation-time ($\lambda_1 = \frac{\eta_{p0}}{G_0}$, where G_0 is the elastic modulus at zero shear-rate), and a characteristic rate-scale (U/L). The non-dimensional group Weissenberg number may be recast, by using the commonplace definition of flow-rate, i.e. $Q = AU = \pi L^2 U$, as $Wi = \lambda_1 \frac{Q}{\pi L^3}$. With this *Wi*-definition one is able to increase elasticity and non-linearity by a couple of ways when the characteristic geometry length-scale L is defined; i.e. one may increase viscoelasticity by increasing the characteristic-time of the fluid λ_1 at fixed Q, or via a Q-increase protocol at fixed λ_1. In this work, we opt for fixing the characteristic-time of the fluid as $\lambda_1 = 1$ s, and promote flow, and hence viscoelastoplastic response, through an incremental-Q steady-state solution-acquisition procedure. Consequently, such definitions render the possibility of analysing flow-response in terms of either *Wi* or Q interchangeably. Armed with such definitions, a general space-time differential statement for the stress equation-of-state may be expressed as:

$$Wi \overset{\nabla}{\boldsymbol{\tau}}_p = 2(1-\beta)\boldsymbol{D} - f\boldsymbol{\tau}_p, \tag{3}$$

where, the upper-convected derivative of extra-stress, $\overset{\nabla}{\boldsymbol{\tau}}_p = \frac{\partial \boldsymbol{\tau}_p}{\partial t} + \boldsymbol{u}\cdot\nabla\boldsymbol{\tau}_p - \nabla\boldsymbol{u}^T\cdot\boldsymbol{\tau}_p - \boldsymbol{\tau}_p\cdot\nabla\boldsymbol{u}$, appears on the lhs of Eq. (3), modulated by the elastic-response of the material through *Wi*, and material structure is incorporated through the structural pre-functional (f) producting the polymeric stress itself, $\boldsymbol{\tau}_p$.

2.1. BMP+_τ_p model approximation

Under derivation through the Bautista–Manero-Puig BMP-family of thixotropic constitutive models, the non-linear structure f-functional is related explicitly to the viscosity of the fluid. Indeed, the f-functional represents a dimensionless fluidity ($f = \frac{\eta_{p0}}{\eta_p}$, inverse viscosity); see [4–8]. In the present study, a novel and revised model-variant is proposed, via the *so-called* BMP+_τ_p model [38]; an advance on the previous BMP model [1,2]. This new BMP+_τ_p model enjoys the benefits of the inclusion of a relaxation-time λ_1 (elasticity) in the fluid-structure construction-destruction dynamics [4–8], whilst retaining a modified non-linear destruction-term. These BMP+_τ_p features provide simultaneously two key experimental-manifestations in wormlike micellar and concentrated polymer solution rheology: first, a bounded extensional-viscosity η_{Ext}-response; and secondly, a first normal-stress in shear $N_{1\,Shear}$ with upturn at high deformation rates (the former is the advance upon the original BMP model).

For the thixotropic BMP+_τ_p micellar model, evolution of the structure dynamic f-functional follows the partial differential equation:

$$\left(\frac{\partial}{\partial t} + \boldsymbol{u}\cdot\nabla\right) f = \frac{1}{\omega}(1-f) + \left(\xi_{G_0} Wi - \xi f\right)\left|\boldsymbol{\tau}_p : \boldsymbol{D}\right|. \tag{4}$$

In the above, the dimensionless micellar-structure coefficients appear in Eq. 4. These account for structural construction ($\omega = \lambda_s \frac{U}{L}$, a time constant) and structural destruction (via $\xi_{G_0} = \frac{k_0 G_0}{\eta_\infty + \delta}(\eta_{p0} + \eta_s)$ and $\xi = k_0(\eta_{p0} + \eta_s)\frac{U}{L}$; two stress constants). Here, λ_s represents the characteristic time of structure-construction, k_0 is the inverse of the structure-destruction stress and $(\eta_\infty + \delta)$ is the viscosity of the polymer at high deformation-rates. One notes in addition, that ABS-f-correction is enforced (see [5–8] for detail), to ensure both physically consistent viscosity estimation and at the same time enhanced numerical tractability.

First, one may reflect on current advances in *constitutive model development for the micellar BMP-family of fluids*, and their ever-improving rheological properties accorded thereby. The original BMP model lacked finite extensibility (infinite-η_{Ext} at finite strain-rates), whilst attractively, $N_{1\,Shear}$ rose at high shear-rates [1,2]. Subsequent BMP model modifications of Boek et al. [3] led to MBM models, corrected for η_{Ext}-unboundedness, by simplifying the destruction-term in Eq. (4), yet inheriting as a consequence, a *retrograde flattening* in $N_{1\,Shear}$ to a terminating plateau at high shear-rates. Shifting attention to pressure-drops and model predictions under complex flows, the MBM model was subsequently found inadequate in producing consistent *epd*-predictions towards the theoretic Stokesian limit (see findings for 4:1:4 contraction-expansion flow [4]). This position was then resolved through NM_τ_p and NM_T model-variants [4–8], by including viscoelastic description (via the relaxation-time λ_1) within the fluid-structure dynamics (Eq. 4). Finally, on this basis, the undesirable *flattening* in $N_{1\,Shear}$ was addressed and corrected for under the present BMP+_τ_p form. This implies that sustained viscoelastic influence is anticipated to apply, as one explores mid to large deformation-rates.

2.2. de Souza Mendes (dSM) model approximation

The original de Souza Mendes model was presented in dimensional total-stress form, coupled with an evolutionary partial differential-equation for material-structure λ to govern the dynamics [9–11]. In the current study, as in [7], the dSM stress equation is re-cast into a split form $\mathbf{T} = \boldsymbol{\tau}_s + \boldsymbol{\tau}_p$, in which the solvent-contribution $\boldsymbol{\tau}_s$ is of constant viscosity Newtonian-type. The polymeric-stress component may then be rearranged to obtain:

$$Wi \overset{\nabla}{\underset{p}{\boldsymbol{\tau}}} = 2\frac{(1-\beta)}{\lambda^m}\boldsymbol{D} - f\boldsymbol{\tau}_p, \tag{5}$$

where the f-functional is defined as $f = \frac{1}{\lambda^m}(\eta_{p0}/\eta_p)$, the polymeric viscosity is $\eta_p(\lambda) = (\frac{\eta_{p0}}{\eta_s})^\lambda - 1$, and a structural modulus is $\frac{G_s(\lambda)}{G_0} = \frac{1}{\lambda^m}$. Note,

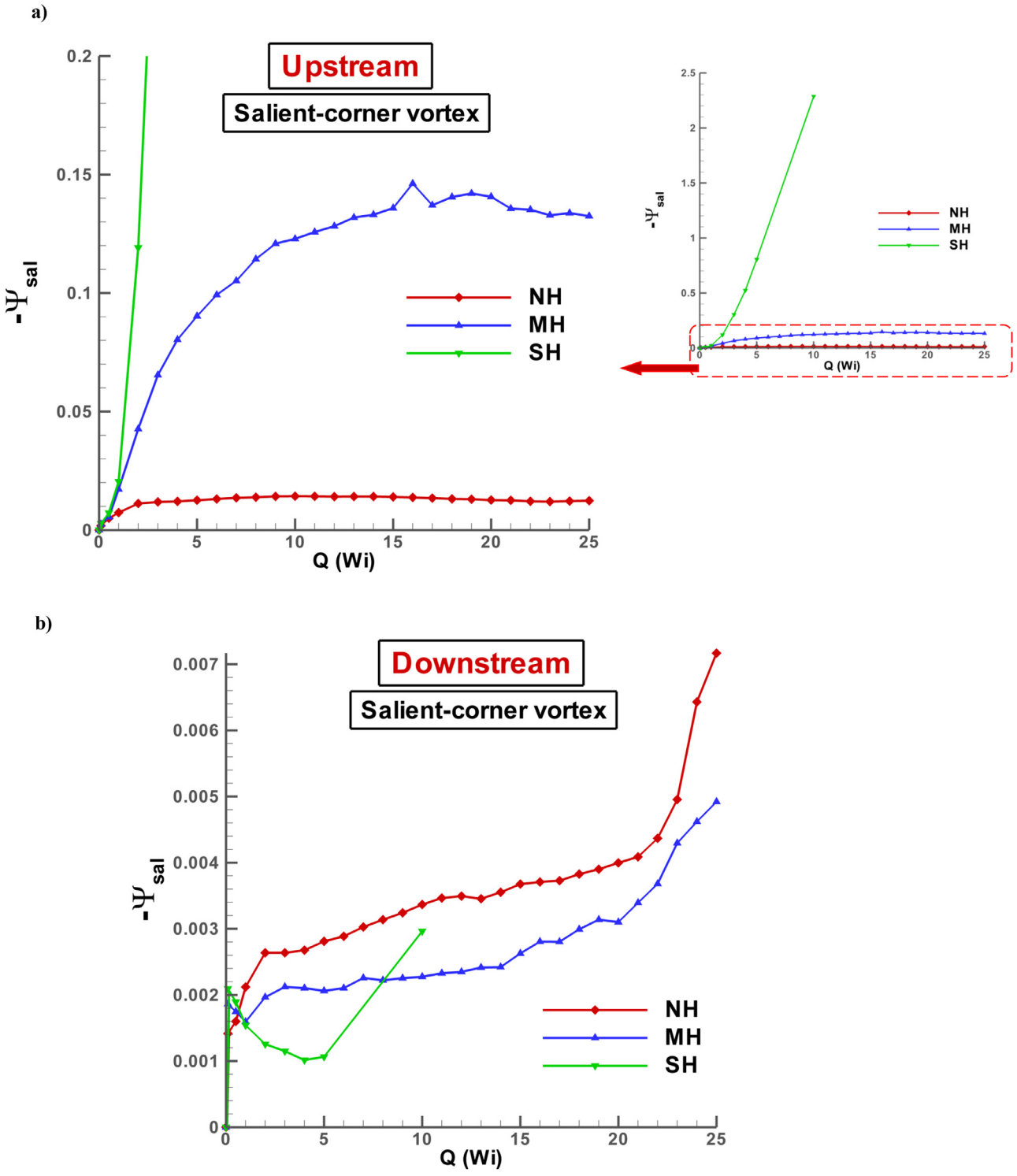

Fig. 6. Salient-corner vortex-intensity ($-\Psi_{sal}$) against flow-rate Q; BMP+_τ_p; a) upstream; b) downstream; hardening comparison: NH $\{\omega, \xi_{G0}\}=\{4, 1\}$, MH $\{\omega, \xi_{G0}\}=\{4, 0.1125\}$, SH $\{\omega, \xi_{G0}\}=\{0.28, 0.1125\}$, $\beta=1/9$.

and unique to this model, the structural-parameter (λ) dictates response in both viscosity and elastic modulus. It appears as an inverse factor in the dissipation-term in Eq. 5, but also within the f-functional and the shear-modulus definitions. This suggests a more complex dSM fluid-structure/material-property dependency. That is, as opposed to the BMP-class of fluids, whose structural f-functional defines a much simpler dimensionless fluidity, appearing only as a multiplying factor on stress in Eq. (3). The interpretation is that the powered-form of the dSM structure-parameter, products and amends the viscoelastic contributions in Eq. (5), via the term $\lambda^m Wi$.

Accordingly, the dSM structure-parameter evolution equation for λ is:

$$\left(\frac{\partial}{\partial t}+\boldsymbol{u}\cdot\nabla\right)\lambda=\frac{1}{\omega_{DS}}\left[(1-\lambda)^a+(1-\lambda_{ss})^a\left(\frac{\lambda}{\lambda_{ss}}\right)^b\right], \tag{6}$$

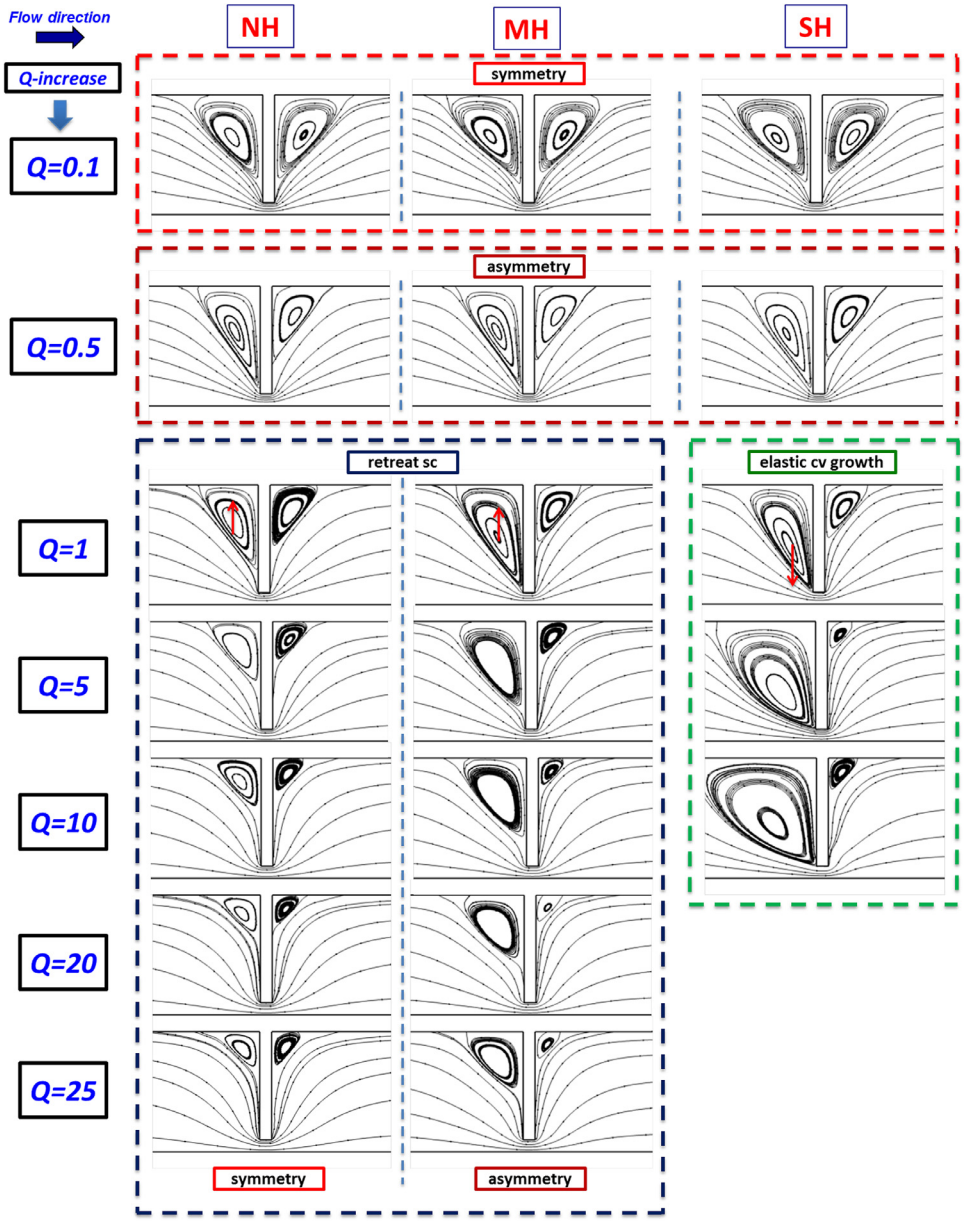

Fig. 7. Streamlines against flow-rate Q and hardening level {NH, MH, SH}; BMP+_τ_p, $\beta = 1/9$.

where, $\omega_{DS} = t_{eq}U/L$ is a dimensionless time-parameter for λ, and, t_{eq} is a characteristic-time for structure-equilibrium. As such, Eq. (6) states a new and corrected form of dSM structure-equation, following [11] whilst correcting for destruction term inconsistency. In brief, Eq. (6) omits a second-invariant multiplicative factor on the destruction term (i.e. $\frac{II_{\tau_p}}{\eta_p(\lambda) II_D}$, which is replaced here by unity). This correction was performed by de Souza Mendes and Thompson [11] for consistent structure-parameter λ–prediction under shear-flow conditions, as reported. Although in complex flow omission of this dimensionless-stress factor can trigger instability (unboundedness in extension), such a factor becomes unity under ideal steady-state flow, and hence should not greatly affect predictions in the vicinity of such state (see on to results and earlier tractability issues arising with this dSM model over the BMP + _τ_p model). The exponents a, b and m are dimensionless positive constants; all taken here as unity in the present implementation. Then, the steady-state structure-parameter λ_{ss} is defined as:

$$\lambda_{ss}(II_{\boldsymbol{D}}) = \frac{\ln \eta_{ss}(II_{\boldsymbol{D}}) - \ln \eta_s}{\ln \eta_{p0} - \ln \eta_s}, \tag{7}$$

and the steady-state viscosity η_{ss} is:

$$\eta_{ss}(II_{\boldsymbol{D}}) = \left[1 - \exp\left(-\frac{II_{\boldsymbol{D}}}{\tau_0}\right)\right]\left[\frac{\tau_0 - \tau_{0d}}{II_{\boldsymbol{D}}} \exp\left(-\frac{II_{\boldsymbol{D}}}{\dot{\gamma}_{0d}}\right) + \frac{\tau_{0d}}{II_{\boldsymbol{D}}} + K {II_{\boldsymbol{D}}}^{n-1}\right] + \beta. \tag{8}$$

In Eq. (8) above, the dynamic and static yield-stress parameters are τ_0 and τ_{0d}, respectively; $\dot{\gamma}_{0d}$ is the shear-rate that denotes the transition between τ_0 to τ_{0d}. Then, K and n are consistency and power-law index, respectively. In complex flow and according to common convention, the generalised second invariant of rate-of-deformation is taken as $\mathrm{II}_{\boldsymbol{D}} = \sqrt{\frac{1}{2} tr \boldsymbol{D}^2}$. Presently, τ_0 and τ_{0d} are equated, simplifying the expression for $\eta_{ss}(II_{\boldsymbol{D}})$. One notes the physics here, that τ_{0d}-variation influences steady-state conditions through $\eta_{ss}(II_{\boldsymbol{D}})$, and hence $\lambda_{ss}(II_{\boldsymbol{D}})$. This has

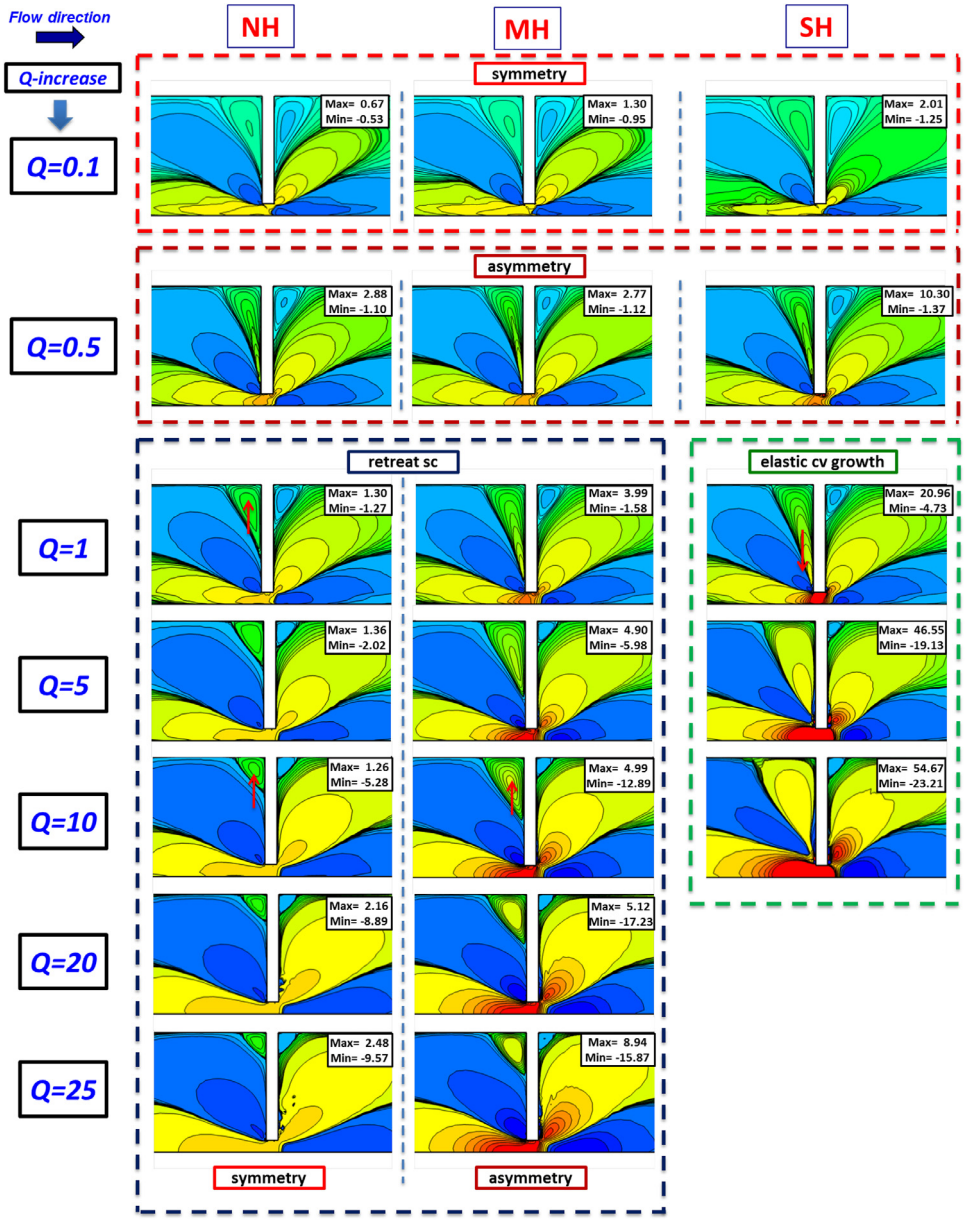

Fig. 8. First normal-stress difference N_1 against flow-rate Q and hardening level {NH, MH, SH}; BMP+_τ_p, $\beta = 1/9$.

impact on the structure-parameter λ, which influences viscosity through its index power of the polymeric viscosity $\eta_p(\lambda) = (\frac{\eta_{p0}}{\eta_s})^{\lambda} - 1$.

2.3. Material functions

Fig. 1 Benchmark highly-polymeric $\beta = 1/9$; BMP+_τ_p model - *hardening comparison*. Comparison across extensional-viscosity η_{Ext}-hardening response; No-Hardening (NH), Moderate-Hardening (MH) and Strong-Hardening (SH) fluids. Note that strain-hardening (Fig. 1a) is accompanied by increase in shear-stress-T_{rz} levels (Fig. 1b), and through first normal-stress difference (Fig. 1c), in $N_{1\,shear}$-plateaux at moderate-to-high shear-rates. Such rheological response adjustment is driven via the variation of thixotropic internal-structure parameters (see Figs. 1–4). This is also patent on comparison across models (see on), when matching $N_{1\,Shear}$-plateaux and extensional viscosity peaks.

Fig. 2 *Polymer-concentration* $(1-\beta)$*-variation*; BMP+_τ_p model; SH matching η_{Ext}-peak across solvent-fractions. Effects of polymer-concentration $(1-\beta)$-variation in second-Newtonian plateaux are exposed, in both shear and extensional deformation (Fig. 2a). Across β-change, T_{rz} only departs from its linear-trend at shear-rates $\lambda_1\dot{\gamma} \sim 3$ units (Fig. 2b). In contrast and interpreted through polymer-concentration $(1-\beta)$-increase, the low shear-rate quadratic-$N_{1\,shear}$ response, slightly shifts to the left elevating early $N_{1\,shear}$-response (Fig. 2c); whilst at higher shear-rates, $(1-\beta)$-rise provokes a shift to the right delaying later $N_{1\,shear}$-response. At intermediate rates, fixed SH-features across polymer-concentrations provide a common $N_{1\,shear}$-plateau at $\sim 10^2$ units.

Fig. 3a-b *Comparison across BMP+_*τ_p *and dSM models*; highly-polymeric solvent-fraction $\beta = 1/9$; NH, matching $N_{1\,shear}$-inflection-points at intermediate shear-rates across models. Here in Fig. 3a, η_{Ext}-hardening is suppressed and $N_{1\,shear}$ differences are exposed from $\lambda_1\dot{\gamma} \sim 1$ units onwards (Fig. 3b), from the viewpoint of a matching inflection-point at $N_{1\,shear} \sim 0.5$ units. From such a station and with rate-rise, BMP+_τ_p provides for an extended $N_{1\,shear}$-plateau response; whilst the dSM-form is more responsive, with immediate rise in $N_{1\,shear}$. Fig. 3c-d data introduces strain-hardening/softening features through the MH

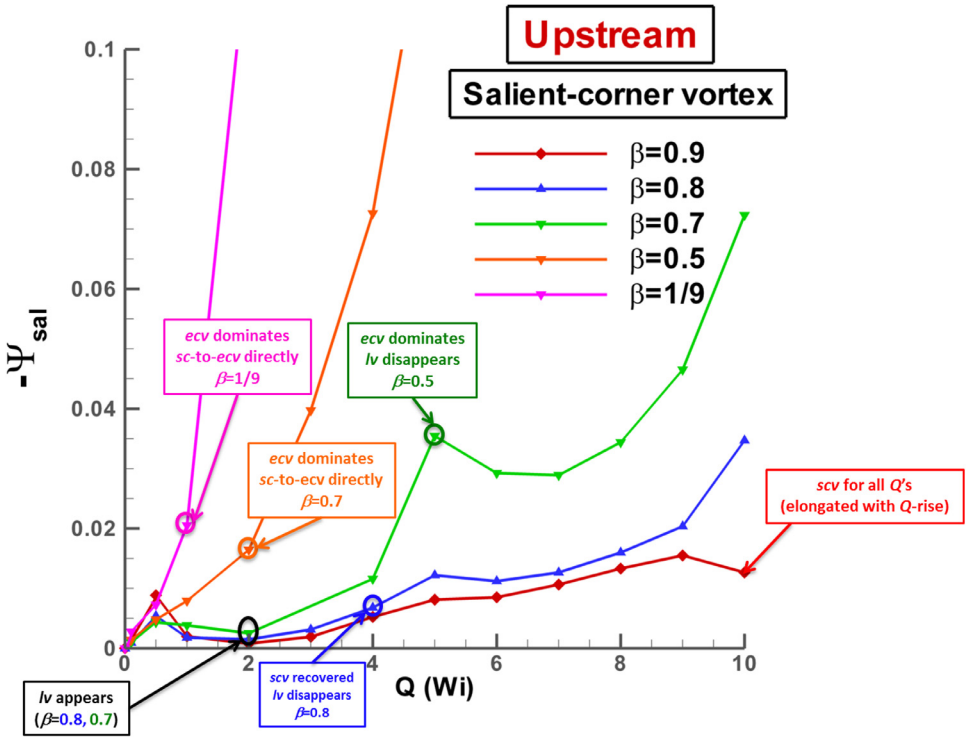

Fig. 9. Upstream salient-corner vortex-intensity (Ψ_{sal}) against flow-rate Q; BMP+_τ_p; solvent-fraction β-variation $\beta = \{0.9, 0.8, 0.7, 0.5, 1/9\}$, SH fluids.

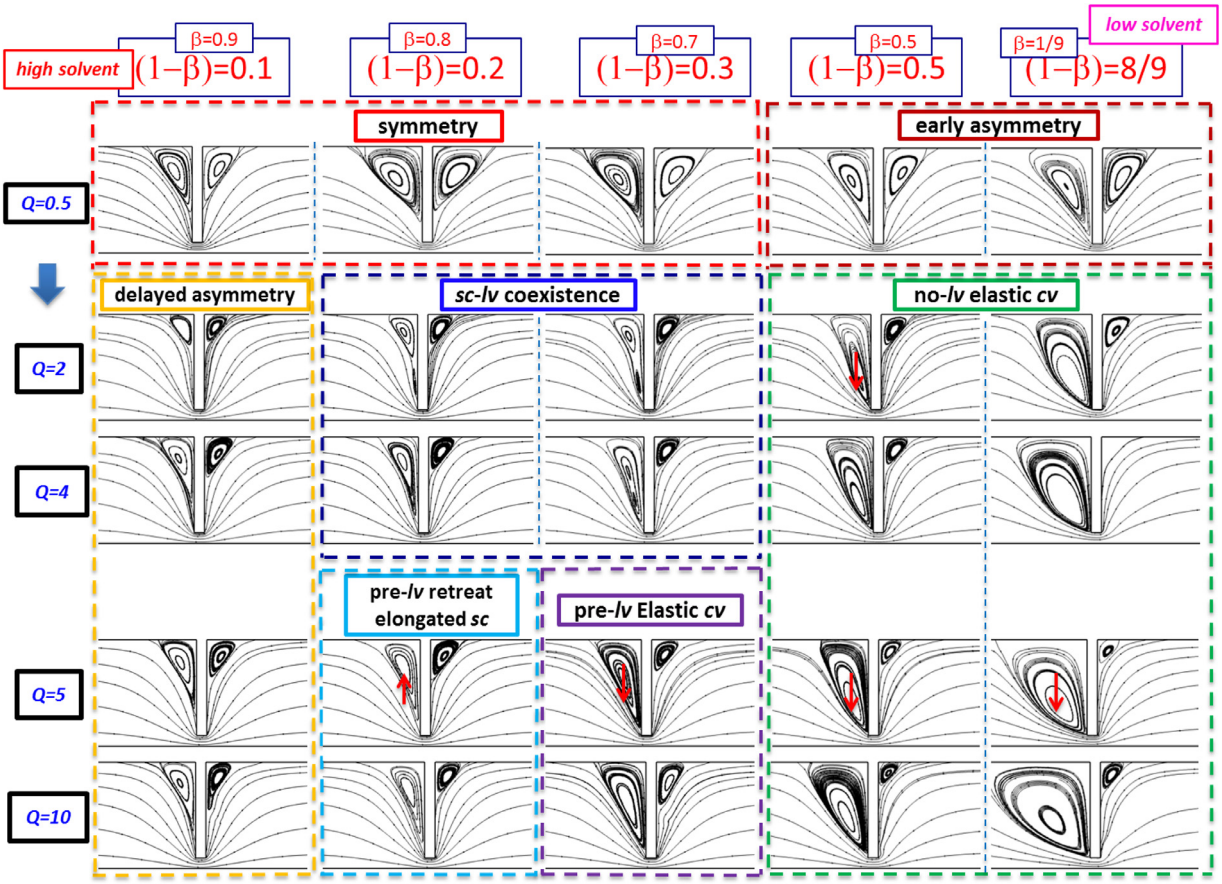

Fig. 10. Streamlines against flow-rate Q and solvent-fraction β-variation $\beta = \{0.9, 0.8, 0.7, 0.5, 1/9\}$, SH fluids; BMP + _$\tau_p$.

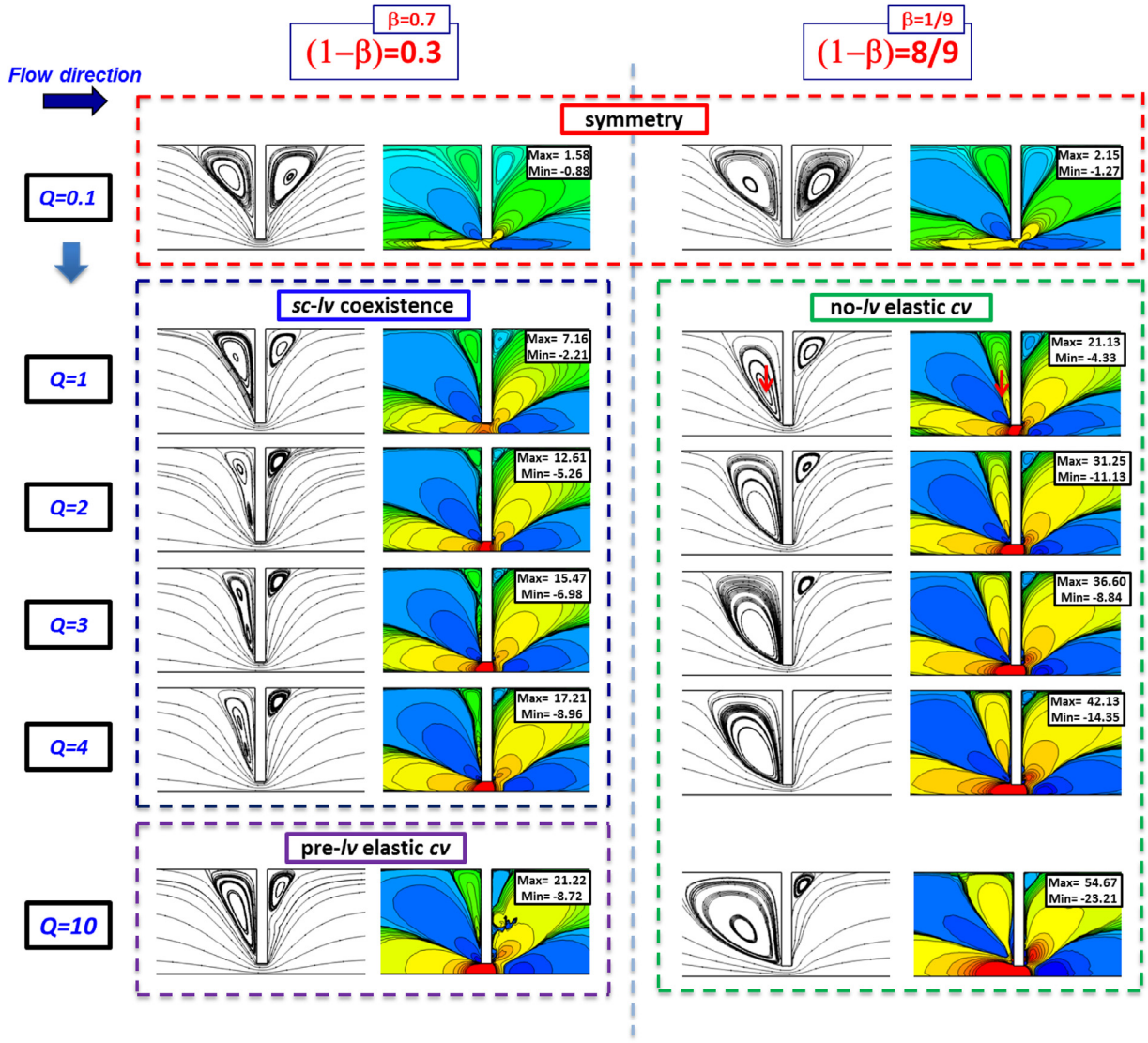

Fig. 11. Streamlines and N_1 against Q and β-variation $\beta = \{0.7, 1/9\}$, SH fluids; BMP+_τ_p.

η_{Ext}-setting (preserving model comparison and polymer-concentration). In this case, a match to and consequence of an increased N_{1shear}-inflection-point (~4.5 units) is sought (Fig. 3d). Notably in this instance, the dSM approximation provides unbounded η_{Ext}-response (Fig. 3c) – hence, large extensional response would be anticipated in extensional deformation.

Fig. 3e-f *Comparison across BMP+_τ_p and dSM models*; *intermediate solvent-fraction* $\beta = 0.7$; SH, matching η_{Ext}-peak across models (Fig. 3e). Here, significant N_{1shear} differences are highlighted, in terms of the level at which the inflection-point departs from the initial quadratic-trend (Fig. 3f). Comparing and contrasting response in N_{1shear} plateaux, BMP+_τ_p N_{1shear} plateaus over an extended rate-range ($30 \leq \lambda_1\dot{\gamma} \leq 3\times10^5$); whilst dSM N_{1shear} possesses a short plateau-window only, due to its relatively early rise at $\lambda_1\dot{\gamma}\sim1$ units.

Fig. 4 *BMP+_τ_p and dSM models in the plastic regime* To expose plastic features, characteristic scaling on viscosity (and on stress, consequently) is chosen based on the second-Newtonian plateau for both models. Recall in this work, yield-stress solid-like features are promoted - for dSM models, via the dynamic yield-stress parameter τ_{0d}; whilst BMP+_τ_p modulates solidification through solute-concentration $(1-\beta)$-increase. Here, BMP+_τ_p yield- stress features appear marked at extremely-high polymer content ($\beta \leq 1/9$; as common yield-stress fluids appear experimentally). This lies in distinct contrast to data in Figs. 1–3, for which the solvent-fraction β–change covers more dilute-fluids ($1/9 \leq \beta \leq 0.9$), representative of conditions for typical viscoelastic response at larger flow-rates. In Fig. 4, contrasting *viscosity-response* is observed with yield-stress elevation across models. Considering shear and extensional viscosities (Fig. 4a and d), one notes that both BMP+_τ_p and dSM models display plastic features in the form of an apparent yield-stress, in which a relatively large but finite first Newtonian viscosity-plateau is predicted [45,46]. Here, the level-separation between the first and the second Newtonian plateaux for both models is over an order-of-magnitude difference. For dSM, τ_{0d}-increase shifts the drop from their first Newtonian-plateaux to larger deformation-rates (Fig. 4a). In contrast, BMP+_τ_p response is witnessed through a significant rise in the first Newtonian-plateau (Fig. 4d). These conspicuous differences are reflected in *shear-stress* T_{rz} patterns observed at low rates. BMP+_τ_p T_{rz} patterns branch out at low deformation-rates and rise with $(1-\beta)$-increase (Fig. 4e). In contrast in Fig. 4b, dSM forms reflect unified closed-patterns at low rates (still lower τ_{0d}would not substantially alter this position). With τ_{0d}-rise and at larger shear-rates, such an unified initial linear response gradually weakens; so, for example, departure occurs at a relatively ear-

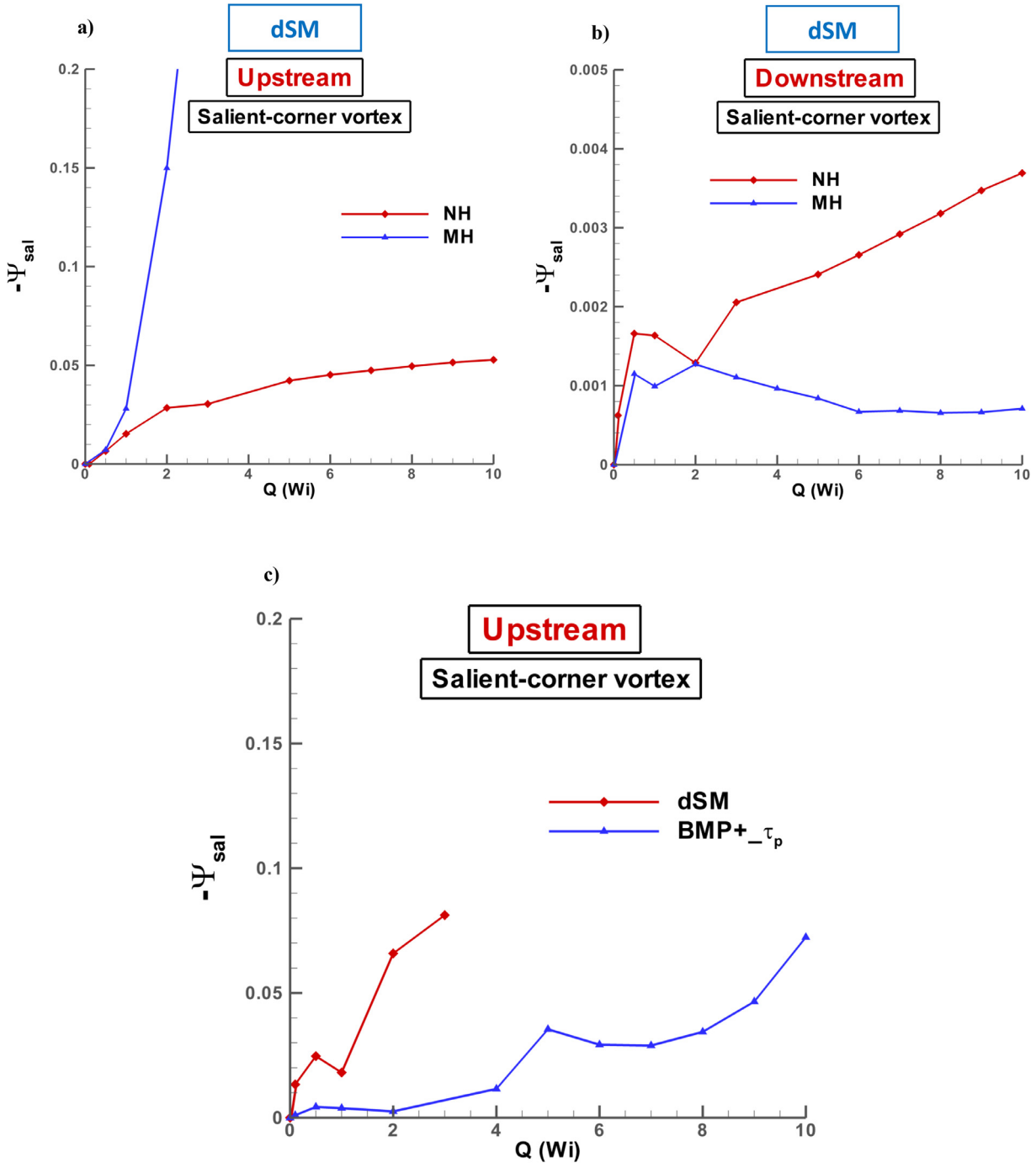

Fig. 12. Salient-corner vortex-intensity ($-\Psi_{sal}$) against flow-rate Q; dSM match of $N_{1\,Shear}$-inflection-point(ip), $\beta = 1/9$-{NH, MH} fluids: a) upstream, b) downstream; c) BMP+_τ_p v dSM η_{Ext}-peak match, {$\beta = 0.7$, SH} fluids.

lier {$\lambda_1\dot{\gamma}$~0.30 units, $\tau_{0d} = 0.02$}, whilst non-linearity is observed at the shear-rates of {$\lambda_1\dot{\gamma}$~1 units, $\tau_{0d} = 1$} (Fig. 4b), thus sustaining tougher fluids (with relatively larger stresses) at larger deformation-rates with dynamic yield-stress τ_{0d}-rise. Response in *first normal-stress difference in shear* $N_{1\,Shear}$ follows likewise, with branching-patterns at low rates for BMP+_τ_p, *but not* dSM. Yet, worthy of note at intermediate shear-rates, is the exaggerated dSM $N_{1\,Shear}$ non-linearity and strength promoted via τ_{0d}-increase (Fig. 4f). In contrast, BMP+_τ_p $(1-\beta)$-increase at these same intermediate shear-rates provokes constant plateaux, with ever-rising levels (Fig. 4c).

3. Flow domain, boundary conditions, VGR-correction and *fe − fv* scheme

The *flow domain* is a circular contraction-expansion of *aspect-ratio* $\alpha = 10$, with sharp-corners. This geometry has been selected due to its strong potential to promote interesting and varied vortex structures at larger flow-rates, and to detect the impact that the present rheological difference across models has on these structures. Details in mesh characteristics can be found in [13]. In order to attain predictive solutions in such highly non-linear situations (recall the extremely low solvent-

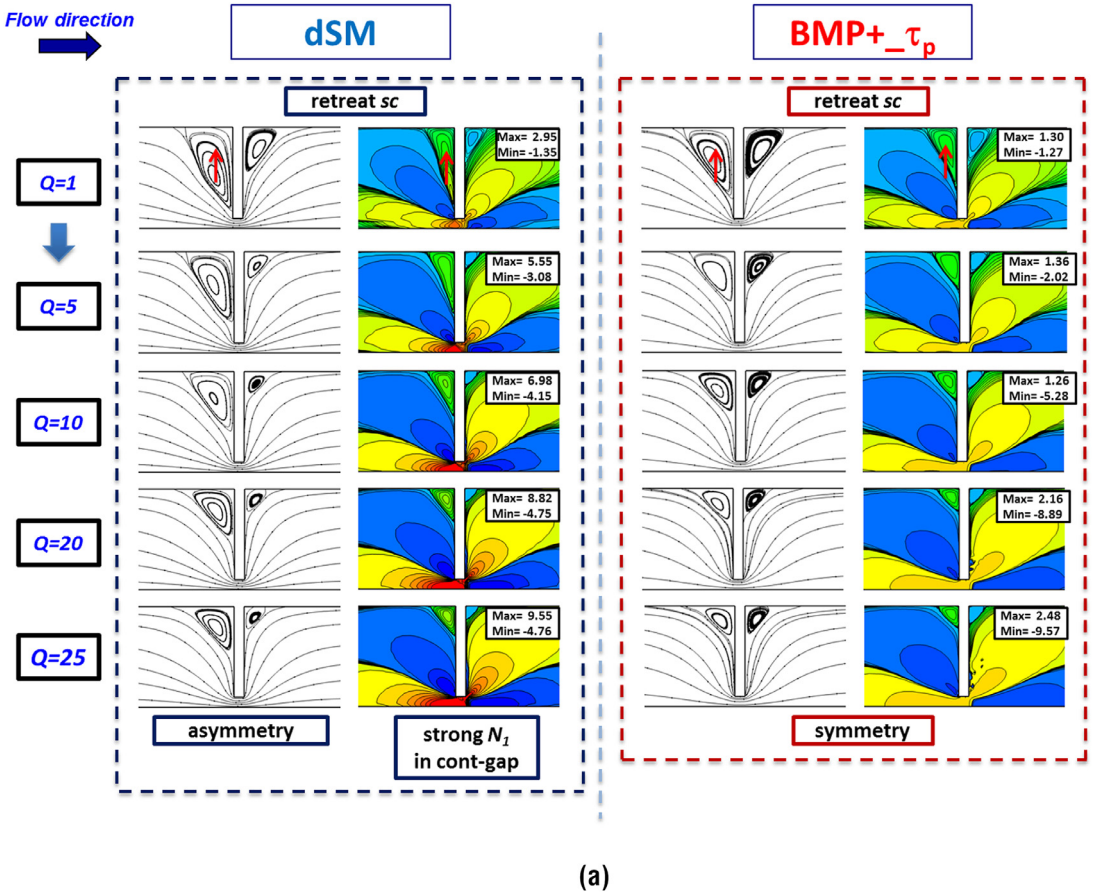

Fig. 13. Streamlines and N_1 against Q; dSM v BMP+_τ_p; a) $\beta = 1/9$, NH fluids; b) $\beta = 1/9$, MH fluids; c) $\beta = 0.7$, SH fluids.

fractions of $\beta \leq 10^{-2}$ and high flow-rate Q-requirements), the stability-enhancing ABSolute f-functional (*ABS-f*) correction and the Velocity-Gradient Recovery (*VGR*) correction are found necessary. Here, *ABS-f* correction enhances numerical tractability through regularisation, by enforcing consistent material property estimation (following the Second Law of Thermodynamics; [5–8]). The *ABS-f*-correction acts within the constitutive equations, adopting the absolute value of the network-structure f-functional (often used to define macroscopic properties; as in non-Newtonian viscosity and non-Hookean elastic modulus [27]). This correction procedure finds general applicability, for example - through the dissipation-function in Bautista–Manero fluids, or in other models through the trace of polymeric-stress, as in PTT and FENE models [5]. There, use of *ABS-f*-correction gave an increase of three orders-of-magnitude in critical Weissenberg number solution attainment. Then, *VGR*-correction imposes shear-free inhomogeneous uniaxial-extensional deformation along the centreline through its velocity-gradient components, in addition to a generalised continuity-conservation condition that is satisfied exactly throughout the flow domain (see also [47–50] more generally for velocity-gradient recovery implementation and procedures). Such a VGR-correction strategy prevents proliferation of numerical discretisation error, originating from the evolving symmetry-line solution, and its amplification with the strengthening of non-linearity (in this case, promoted by flow-rate, polymer-concentration and yields-stress increase; [5–8]).

The increasing-Q protocol itself demands some care with respect to accurate boundary condition implementation between subsequent flow-rates, which is affected by the strong shear-thinning features of highly-polymeric fluids in the moderate-to-high flow-rate regime. Hence, *to ensure consistency between the outlet (also inlet) boundary and its corresponding internal-field neighbourhood*, a regional-solution *outlet-feedback (also inlet-feedforward) procedure* is performed per time-step. This is implemented *on polymeric-stress* $\boldsymbol{\tau}_p$ and *velocity-gradient* $\nabla \boldsymbol{u}$ solution-components [8], extracting overwrite nodal-values from fully-developed locations downstream (or upstream) of the obstruction, as appropriate. During the continuation incrementation-procedure through steady-state Q-solutions, the streamwise *velocity* u_z *boundary condition is handled* by *an initial feedback-feedforward step at the outset of each new* Q-solution stage [8]. In this, an internal-domain fully-developed u_z-profile is taken from a previous (but close) steady-state Q-solution, subsequently rescaled accordingly, and then set at inlet-outlet locations for the present flow-rate solution. This procedure is equivalent to setting steady-simple shear flow boundary conditions at each flow-rate. Moreover, such u_z-profile rescaling implies a change in the characteristic velocity U per flow-rate Q, and accordingly, via $Wi = \lambda_1 U/L = \lambda_1 \frac{Q}{\pi L^3}$, a different associated Wi-level.

Hybrid finite element/finite volume scheme This hybrid space-time algorithmic scheme has time-stepping and fractional-staged equation structure, see [47–50]. Finite-element (*fe*) discretisation is invoked on the momentum-continuity equation doublet of incremental pressure-correction form, whilst finite-volume (*fv*) discretisation is instigated on the constitutive stress-equation. This choice respects equation-type specification. Hence, Galerkin-type (*fe*) specification is selected for momentum-continuity on triangular tesselations, with subtended subcell/cell-vertex finite-volume (*fv*) discretisation for stress. This leads to a space-efficient element-by-element iterative solution procedure for all but the pressure-equation, which itself is resolved with a direct Choleski-reduction method. The (*fv*) component for stress, then collapses into a direct single-iteration implementation. The temporal conservation-form equation for stress is non-linear with inhomogeneous source terms, and as such requires both fluctuation-distribution for

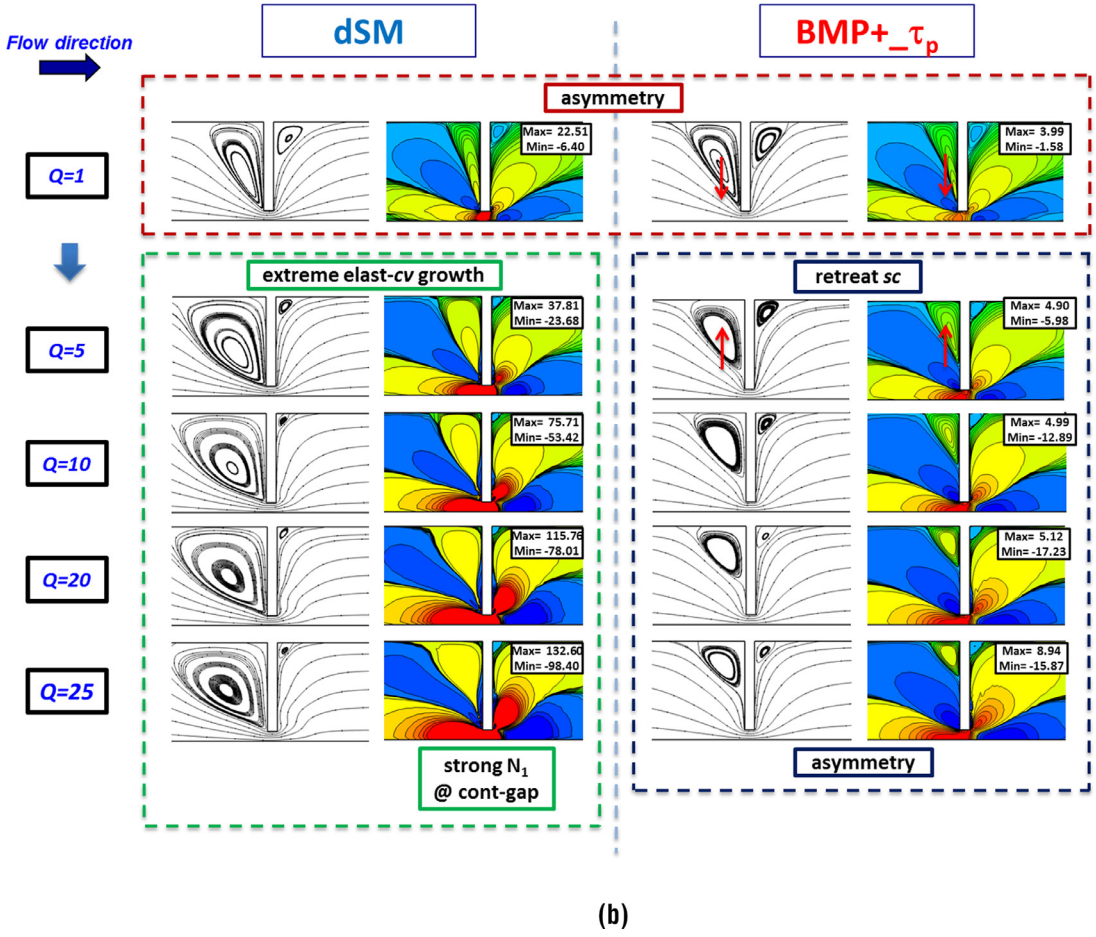

Fig. 13. Continued

fluxes (upwinding) and median-dual-cell treatment for source terms. On the parent *fe* triangular-cell grid, velocity interpolation is quadratic, alongside linear interpolation for pressure. Then, the subtended subcell *fv*-triangular-tessellation is constructed by connecting the mid-side nodes of the parent cells (four subcells per parent cell). In such a structured tessellation, stress variables are located at the vertices of *fv*-subcells and hence solution interpolation between various equation stages is avoided. This provides for a subcell-vertex *fv*-method, equivalent to linear interpolation on trial-solutions, but at the child subcell-level. The corresponding schema developed is second-order accurate and consistent in time [48, 49].

4. Results

As depicted in Fig. 5 and for illustrative purposes, the findings of this research work have been sectioned into two flow-regimes: a viscoelastic regime and a plastic regime. Section 4.1 *Viscoelastic Regime* is focused on the fluidised response with relatively diluted fluids ($1/9 \leq \beta \leq 0.9$) and high flow-rates ($Q \geq 1$). As a main finding, representation of the viscoelastic response is provided in Fig. 5a, where rich flow-structural streamlines (portraying coexistence of salient-corner and lip vortices) intimately correlate with its counterpart normal-stress field, and whose intensity appears correlated to rotational vortex-intensity (see on).

Section 4.2 *Plastic Regime* deals with the solid-like features of the viscoelastoplastic fluids studied. In contrast to the viscoelastic regime, the plastic regime explores the plastic response of dSM and BMP+_τ_p models under extremely solute-concentrated fluids ($\beta \leq 1/9$) and relatively low flow-rates ($Q \leq 10$). Here in Fig. 5b, illustration of such response appears through yield-fronts, made asymmetric due to fluidisation and viscoelasticity.

4.1. Viscoelastic regime – variation in moderate-to-high flow-rates Q and polymer-concentration (1 – β)

4.1.1. BMP+_τ_p Predictions; flow-structure and stress-response

4.1.1.1. Comparison across hardening levels –NH, MH and SH; highly-polymeric ($\beta = 1/9$) under Q-increase. Here, a main observation has been that vortex-phasing is found to be dictated through trends in extensional viscosity. In particular, this lies in agreement with previous findings for Boger fluids [12,13]. In this manner, and by adopting *Q*-increase as the continuation mode between steady-states, the gradual evolution from a salient-corner (*sc*) vortex-pattern is seen to develop into one of an elastic-corner (*ec*) vortex-pattern (see [13,51]). Such an elastic-corner vortex is commonly observed at high flow-rates, where elastic features dominate and this strong kinematic flow-structure occupies the whole of the corner-recess (see vortex-intensity Ψ_{sal}-plots and streamlines in Figs. 6 and 7, respectively). *Counterpart fields of the first normal-stress difference in complex flow* N_1 (Fig. 8) overall reflect the vortex-phasing and internal vortex-structures formed. Moreover, internal vortex-structure development and spatial location is closely related to build-up observed in $N_{1\,Shear}$ (due to the close proximity of the vortex to the wall [13]). Extrema (and colouring) provide a pointer to the localised influence and N_1-structures in the recess-corner flow.

Vortex-intensity across hardening-cases Vortex-intensity Ψ_{sal}-plots are presented in Fig. 6. Across the various hardening-options, η_{Ext}-hardening segregates the rotational-strength of the upstream vortex into three distinct levels. The corresponding field representation of such kinematic-

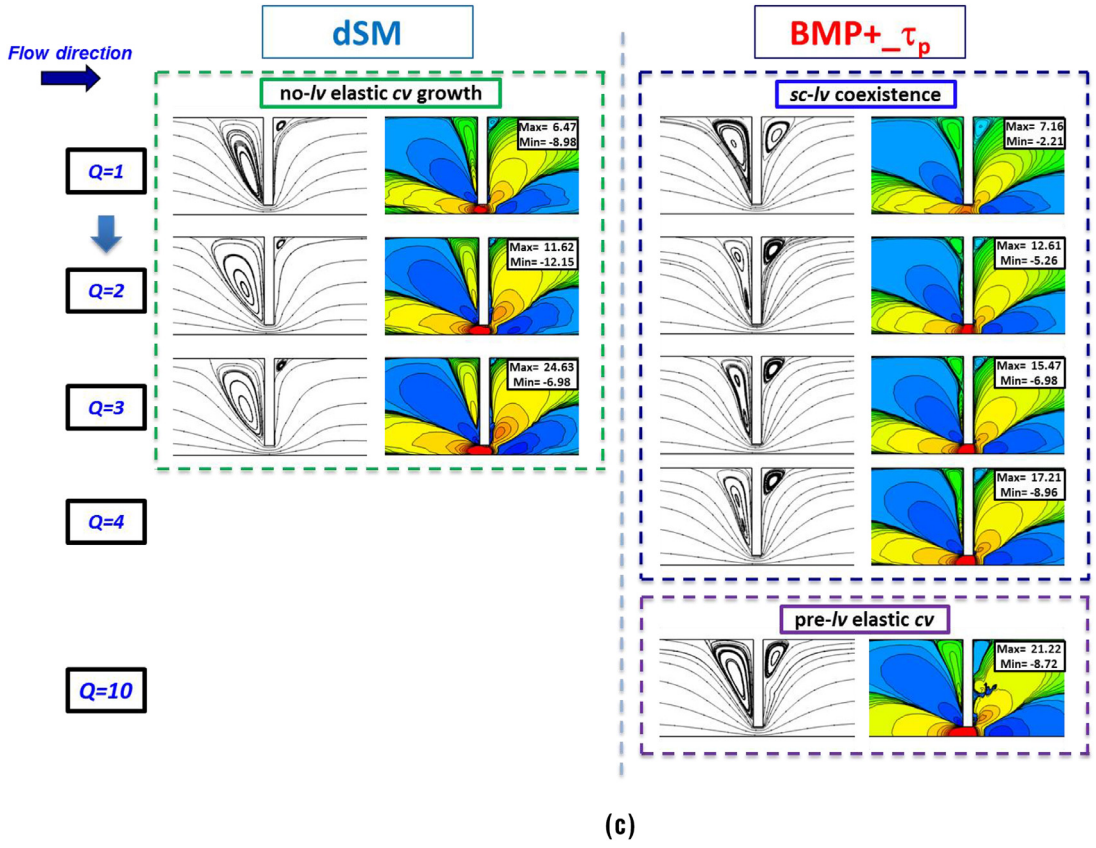

Fig. 13. Continued

structures, both in streamline patterns and N_1-fields, is provided in Figs. 7 and 8, respectively. *Upstream of the contraction*, plateauing Ψ_{sal}-trends are retrieved in No-Hardening (NH) and Moderate-Hardening (MH) cases, whilst Strong-Hardening (SH) Ψ_{sal}-rises sharply (Fig. 6a). NH and MH plateaux differ by an order-of-magnitude in intensity, from NH $\Psi_{sal}\sim0.012$ units, to MH $\Psi_{sal}\sim0.14$ units. Moreover, greater hardening retards the approach in take up of a plateau. For instance, NH plateaus at $Q\sim2$, whilst MH softens its slope at $Q\sim3$, and SH invariably rises. Within such levelling and evolution with Q-rise, *NH-solutions* report some degree of asymmetry for $Q\geq0.5$, followed by vortex-retreat into the salient-corner (see streamline patterns in Fig. 7 and counterpart 2D N_1-field in Fig. 8), and ultimately at high-Q, to symmetric and significantly reduced vortices at $Q\sim25$. In contrast, under *MH-solutions*, marked asymmetry emerges in the range $0.5\leq Q\leq1$ (elongated upstream-vortices and downstream–vortex shrinkage in Fig. 7, with intensification in normal-stress response – indicated in colour transition to yellow-levels in Fig. 8). Then at $Q\sim5$, a plateau is recorded in vortex-size (Figs. 7 and 8; also observed in Ψ_{sal}, see Fig. 6a-top-right), followed by retreat into the salient-corner, producing asymmetric vortex-patterns by $Q\sim25$. The *SH-solution-set* with sustained Ψ_{sal}-rise, attains a striking maximum $\Psi_{sal}\sim2.3$ units at $Q=10$ (see inset Fig. 6a). The SH-flow-structure displays exaggerated asymmetry, with extreme upstream-vortex growth and N_1-enhancement towards the re-entrant corner (of elastic-corner vortex-type), where the rotation-centre is shifted (Figs. 7 and 8). Note that for $Q=10$ SH-solution (last tractable), N_1-enhancement is witnessed by a yellow/intense-positive vortex-like structure, that is detached from the contraction back-face by a blue/intense-negative peak. One notes, this N_1-overshoot-undershoot feature has already been reported for Boger fluids, in the elastic-corner vortex-evolution phase [13]. One may note that across the various hardening instances considered, SH develops a strong red/intense-zone in the contraction-gap, which is weakened under MH, and absent altogether under NH-setting (in agreement with N_1-extrema in Fig. 8).

Across hardening-variants, the upstream-vortex evolution with Q-rise may be clearly linked with fluid-response in ideal deformation. Hence, for the *NH-fluid*, the trend of continual vortex-retreat may be correlated with NH strain-softening properties, whilst also being devoid of any manifestations of hardening (see Fig. 1a); additionally, reduced symmetrical vortices at high-Q are related to the relatively low $N_{1\,Shear}$-levels (Fig. 1c). For the *MH-fluid* and with strain-rate rise, the initial vortex-growth and delayed retreat correlate well with the moderate strain-softening/hardening η_{Ext}-response (Fig. 1a); whilst the asymmetric vortices at large flow-rates may be due to the increased MH $N_{1\,Shear}$-levels (Fig. 1c). Once more, one may recall our earlier findings, where internal vortex-activity matched with $N_{1\,Shear}$, due to vortex proximity to the wall [13]. For these two *NH and MH instances, the attainment of a second Newtonian-plateau regime is conspicuous* (Figs. 7 and 8). Notably, this position generates diminished upstream-vortices, which return to salient-corner forms, whilst adopting asymmetrical orientation about the obstruction and manifesting $N_{1\,Shear}$-strength. Finally, the exaggerated SH asymmetry and elastic-corner vortex formation are in-line with the severe strain-hardening and $N_{1\,Shear}$ features of this SH fluid (Fig. 1a and c).

The relatively *reduced-activity in downstream-vortices* is also worthy of note. In the largest illustration of departure (SH-case), the upstream vortex-activity is two to three orders-of-magnitude more intense than that downstream of the constriction (Fig. 6). In terms of flow-structure and with Q-rise, downstream-vortices balance the upstream activity, by simply shrinking into the salient-corner, whilst increasing in intensity. These observations lie in distinct contrast to the counterpart phenomena revealed experimentally for Boger fluids (high-solvent fractions, constant shear-viscosity and significant elasticity [13]). There, and for constant-viscosity highly-elastic fluids, upstream-vortex en-

hancement is attended at larger rates by similar downstream vortex-activity (with even downstream lip-vortex formation found in larger aspect-ratios $\alpha \geq 6$; [13]). In addition, in Fig. 6b and with respect to upstream observations, an inversion of *downstream* Ψ_{sal}-trend-ordering is recorded. Here, NH downstream-vortices rotate with the largest strength whilst SH-vortices recirculate with the weakest. Under $Q < 20$, downstream NH-vortices rotate more quickly (Ψ_{sal_avg}~0.0034 units), than those of MH (Ψ_{sal_avg}~0.0024 units), and those of SH in the range at $Q <= 5$ (Ψ_{sal_avg}~0.0014 units). Finally at relatively large flow-rates, all hardening-cases display a sudden Ψ_{sal}-rise.

4.1.2. Variation in polymer-concentration $(1-\beta)$

Vortex-intensity with polymer-concentration $(1-\beta)$*-variation* A range of solvent-fractions of $\beta = \{1/9, 0.5, 0.7, 0.8, 0.9\}$ is studied (upstream vortex-intensity Fig. 9; streamlines-N_1 Figs. 10 and 11; ideal response in Fig. 2), under strong hardening SH-conditions, principally with focus upon vortex-phasing (*lip-vortex formation)*.

Under polymer-concentration $(1-\beta)$*-increase*, vortex-intensity Ψ_{sal} is reflected in Fig. 9. In general and *upstream* of the contraction, solute-content $(1-\beta)$-increase elevates the intensity of vortex rotational-speed and segregates response. With Q-rise, Ψ_{sal} appears flatter in solvent-dominated fluids ($\beta = 0.9$), whilst it sharply rises for highly-polymeric fluids ($\beta = 1/9$). This is accompanied by a *change in vortex-cell shape and traversal of rotation-loci* (see last column of Fig. 10). As described under hardening-changes above, diminished *downstream*-activity appears to balance that in the upstream of the contraction, only adjusting with $(1-\beta)$.

For solvent-dominated fluids $(\beta = 0.9)$*,* vortex-*intensity* Ψ_{sal} rises shallowly, levelling at Ψ_{sal}~0.015 units at Q~10 (Fig. 9). Streamline patterns display a retarded upstream-response (first column of Fig. 10), with symmetrical salient-corner (*sc*) vortices in the range $0.1 \leq Q \leq 1$, followed upon further Q-rise ($2 \leq Q \leq 10$) by delayed *sc*-vortex-elongation.

With $(1-\beta)$*-increase, yet still within the diluted-regime* $(\beta = \{0.8, 0.7\})$, Ψ_{sal} is seen to somewhat enhance with Q-increase; in the largest-Ψ_{sal} recorded ($\beta = 0.7$, $Q = 10$), Ψ_{sal} is some 4.5-times larger than that observed in the solvent-dominated $\beta = 0.9$-case (Fig. 9). Conspicuously, in terms of vortex-structure (second and third columns of Fig. 10), after initial symmetrical streamline ($0.1 \leq Q \leq 1$; somewhat distorted with increase in polymer-concentration), *intermediate phases* of salient-corner (*sc*)/lip-vortex (*lv*) *coexistence* are recorded ($1 \leq Q \leq 4$). Notably, *within the high-Q range* of $Q \geq 5$, each $\beta = \{0.8, 0.7\}$ solution-set has an alternative and different response to Q-rise (Fig. 10). Under $\beta = 0.8$, the co-existent sc-*lv* structures coalesce, and a single *sc*-vortex is recovered. In contrast, at slightly increased polymer-concentration ($\beta = 0.7$), the *lv dominates* and becomes an *elastic-corner (ec) vortex*.

Finally under *highly-polymeric fluids* $(\beta \leq 0.5)$, a steep Ψ_{sal}-rise is recorded with incrementation in flow-rate (Fig. 9). The increase in rotational intensity is such that, at $Q = 10$, $\beta = 1/9$-upstream rotational-intensity (Ψ_{sal}~2.29 units) is some 230-times stronger than that under the solvent-dominated $\beta = 0.9$-fluid (Ψ_{sal}~0.01 units) at the same flow-rate. With Q-rise, such strong ($\beta \leq 0.5$)-Ψ_{sal} behaviour is reflected in a *direct transition from salient-corner (sc)- to elastic-corner (ec)-vortex* formation (last two columns of Fig. 10).

The correspondence of flow-structure, through vortex-activity to normal-stress development, is illustrated in Fig. 11. Here, the most active instance of $\beta = 0.7$ is selected for illustration purposes, where salient-corner/lip vortex coexistence is strongly evident. In the $1 \leq Q \leq 4$ range, N_1-fields possess isolated zones in the corner/back-face region, which correspond to counterpart streamline vortices. For $1 \leq Q \leq 3$, upstream salient-corner and lip-vortex-like N_1-patterns are clearly apparent, attended with the corresponding downstream salient-corner N_1-structures. Upstream and for $Q = 4$, an elongated N_1-structure with two centres of rotation is retrieved; one less-intense, located at the salient-corner, and a second more-intense near the lip; this intense lip-vortex structure announces the onset of lip-vortex domination.

4.1.3. BMP+_τ_p vs dSM predictions: Flow structure

The present theme continues to report on contrast in solution response when considering variation across constitutive models, namely through differences observed when appealing to dSM representation against the foregoing BMP+_τ_p form. Three separate instances of prominent rheological distinction are identified. The *first comparison* is taken under highly-polymeric $\beta = 1/9$ and no hardening NH-response, when matching N_{1Shear}-inflection-points. Then, the *second comparison* under moderate hardening MH-response, preserves the match in $\beta = 1/9$ and N_{1Shear}-inflection-point match. The *third comparison* under strong hardening SH-response, matches extensional viscosity η_{Ext}-peaks at intermediate solvent-fraction ($\beta = 0.7$; diluted-fluids). In terms of material-function response and under $\{\beta = 1/9$, NH$\}$, one observes the effects of N_{1Shear}-rise with shear-rate increase (Fig. 3a-b). With $\{\beta = 1/9$, MH$\}$, strain-hardening/softening influence is analysed (Fig. 3c-d). Lastly $\{\beta = 0.7$, SH$\}$ setting, exposes the effects of N_{1Shear}-differences under stronger solvent presence (see Fig. 3e-f).

4.1.3.1. dSM NH-MH-fluids N_{1shear}*-plateaux matching (highly-polymeric* $\beta = 1/9$*).* In Fig. 12a and for complex contraction-expansion flow, vortex-intensity (-Ψ_{sal})-plots are presented, contrasting NH and MH-instances (corresponding to the match in N_{1Shear} inflection-points; see Fig 3a–d). *Upstream* and with Q-rise, NH-Ψ_{sal} plateaus at Ψ_{sal}~0.05 units (Q~10), whilst MH-Ψ_{sal} rises severely. These two distinct trends may be aligned with the NH and MH η_{Ext}-response, for which NH barely displays hardening at intermediate strain-rates (see Fig. 3a); whilst MH displays unbounded response (Fig. 3c). Streamline-patterns reflect these contrasting positions under extension. *Under NH*, dSM approximation exhibits stronger asymmetry than BMP+_τ_p predictions (Fig. 13a). Such solution response is synchronised with a stronger response in normal-stress (compare N_1-extrema across models at fixed-Q; Fig. 3b). Notably, beyond $Q > 5$ in Fig. 13a, upstream-vortex retraction into the recess corner is gathered, in accord with the strain-softening nature of these NH-fluids (see Fig. 3a). In the high-Q regime ($Q = 25$), dSM sharp-asymmetrical vortex-structures contrast with BMP+_τ_p symmetrical-response (Fig. 13a). Such disparity is consistent with dSM stronger elastic-response, with dSM N_{1max} being some four times larger than that of BMP+_τ_p (Fig. 3b). *Once some strain-hardening has been introduced*, dSM MH responds through intensely large-N_1 zones around the constriction-region (see Fig. 13b). Recall that dSM has an unbounded extensional response, when matching N_{1shear}-inflection-points with the MH-BMP+_τ_p fluid (Fig. 3c). Consistently, dSM N_1-extrema grow by an order-of-magnitude above and relative to that for BMP+_τ_p. Through Q-rise, such contrasting extension-driven dSM response, is accompanied by the early development of an elastic-corner vortex; as opposed to that under BMP+_τ_p of vortex-enhancement and subsequent vortex-retraction. Interestingly, now *downstream,* NH-Ψ_{sal} rises continually (Fig. 12b); whilst MH-Ψ_{sal} firstly rises in the $0 < Q \leq 2$ range, locating a maximum of vortex-intensity of -Ψ_{sal}~0.0012 units at $Q = 2$; then beyond $Q = 2$, a gradual Ψ_{sal} decline is observed, to reach an ultimate plateau-level of Ψ_{sal}~0.0006 units.

4.1.3.2. Strong-hardening (SH) fluids, intermediate solvent-fractions $(\beta$~$0.7)$*.* Fig. 13c $\{\beta = 0.7$, SH$\}$ η_{Ext}-peak match – comparison of lip-vortex formation and exposition of N_1-effects. This preliminary examination of representative dSM response now lies in stark contrast to that discussed above for BMP+_τ_p solutions (in Fig. 3e). Under such solvent-fraction setting and hardening intensity, Q-increase BMP+_τ_p solutions disclose an intermediate salient-corner (*sc*)/lip-vortex (*lv*) coexistence phase, followed by elastic-corner vortex formation. In contrast and even from early flow-rates of $Q = 0.1$, dSM solutions develop asymmetry and much stronger upstream *elastic-corner (ec)*-vortices. This departure is strikingly observed in vortex-intensity trends of Fig. 12c. Here, dSM Ψ_{sal}-rises steeply from low flow-rates, in contrast to the relatively softer BMP+_τ_p-trend. For instance, at $Q = 3$ dSM-Ψ_{sal} attains a level of ~0.08 units, which is some eight times larger than

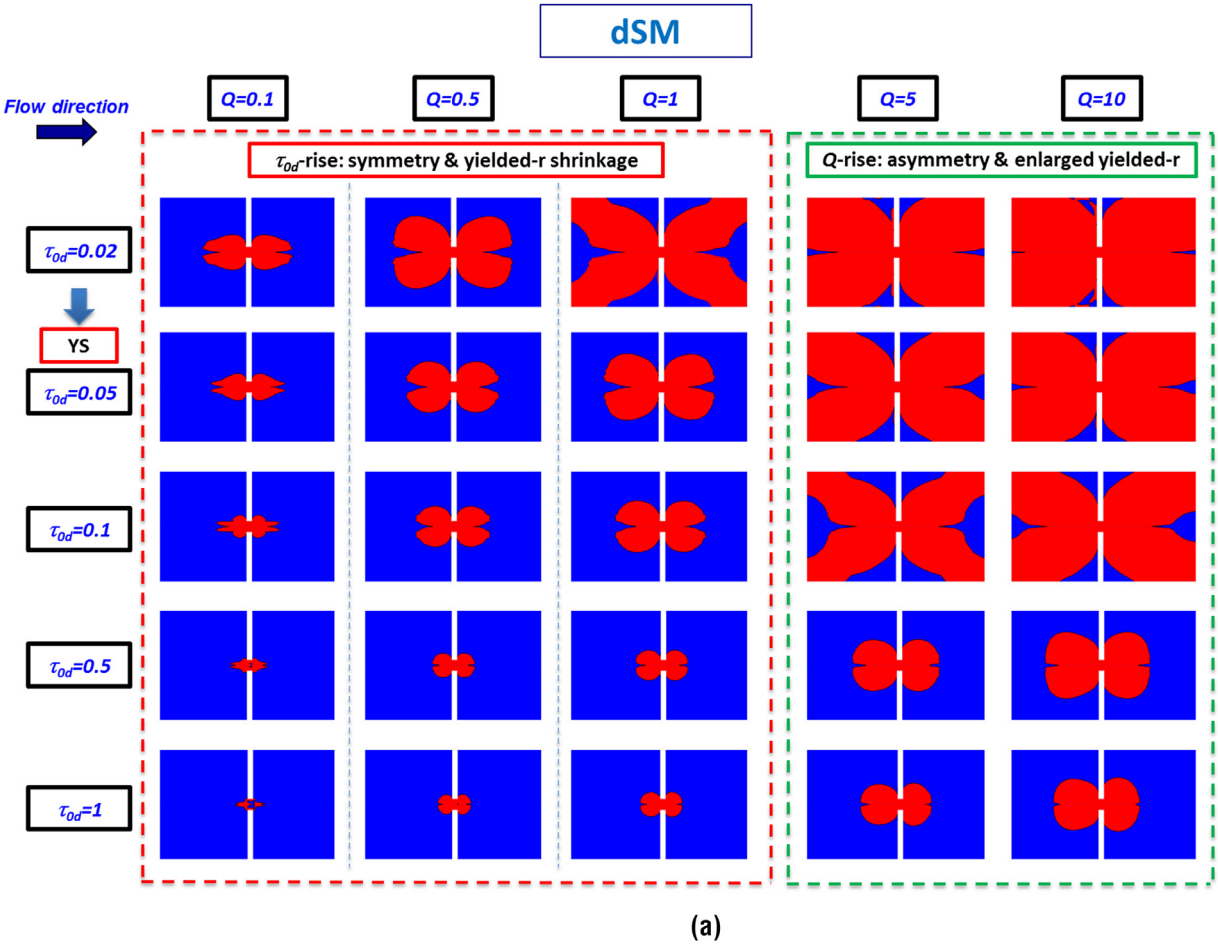

Fig. 14. Yield fronts against Q and yield-stress; a) dSM (τ_{0d}-increase; $\beta = 1/9$), b) BMP+_τ_p (β-increase); MH fluids.

the intensity retrieved for BMP+_τ_p-solution (Ψ_{sal}~0.01 units). Then, such stronger dSM response is also reflected in N_1-field structure and development, for which elongated upstream vortex-like structures emerge (Fig. 13c). Comparatively at each Q-level studied, dSM N_1-extrema are significantly enhanced, as gathered through corresponding red/intense-regions across the contraction-gap, which are stronger and larger than those equivalent for BMP+_τ_p. The final tractable dSM steady-state solution to be extracted is that at $Q = 3$. One may associate the considerably stronger dSM response, noted in ideal shear (reduced shear-thinning) and extension (SH), with this earlier loss in solution tractability against that for BMP+_τ_p.

4.2. The plastic regime-low flow-rates (Q ≤ 10) and extremely high polymer concentrations (β ≤ 1/9); moderate hardening MH-fluids; exposure to yield-stress influence - dSM ($\tau_0 = \tau_{0d}$-increase) against BMP+_τ_p (β-decrease)

4.2.1. Yield-fronts

dSM solutions in the form of yield-fronts are illustrated in Fig. 14a, upon selecting the highly-polymeric concentration ($\beta = 1/9$) to establish a common comparison-basis with BMP+_τ_p predictions. The criterion to discern the *yield-front (interface between yielded fluid and non-yielded solid-like material)* is derived through the second invariant of polymeric-stress, $II_{\tau_p} = \sqrt{\frac{1}{2} tr\boldsymbol{\tau}_p^2}$; as such, stress levels greater than or equal to the II_{τ_p}-threshold correspond to yielded-fluid zones (see [29] for this and other valid measures to discern yield-fronts). At fixed $Q = 1$ and under yield-stress parameters $\tau_0 = \tau_{0d} = 0.02$, an X-shaped yield-front region is identified. This asymmetrical pattern about the contraction-plane, is retrieved from imbalanced unyielded-zones in the recess-corners. Subsequent and rising yield-stress influence ($\tau_{0d} \geq 0.05$), renders shrinking double-claw/shamrock-shaped unyielded regions, which are confined to the contraction-gap neighbourhood. Conversely, with Q-rise, a sequence of fixed-$\tau_{0d} = 0.1$ solutions, commence from a symmetrical eight-petal/branched and yielded-structure, which is confined to the constriction-zone. Then, at an intermediate Q-range ($0.5 \leq Q \leq 1$), the eight-petal structure gives way to a four-petal/shamrock-shaped unyielded-zone. Finally, at relatively high-Q ($Q \geq 5$), the ever expanding yield-fronts of the contraction-flow zone, link-up with those from the upstream-wall and downstream-wall flow regions. At this juncture, elastic-effects become prominent (recall, rising $N_{1\,Shear}$ material-function response; Fig. 3d), with larger asymmetrical upstream yielded-zones appearing in the corner-recess regions.

Comparatively, across models and at low flow-rates, *BMP+_τ_p solutions* (Fig. 14b) reveal similar yield-front response to that of dSM. In contrast however, at higher flow-rates ($Q > 5$) and extremely low solvent-fractions ($\beta \leq 0.005$), ever expanding yielded-regions are recorded, that are slightly more prominent with *BMP+_τ_p* than dSM representation, showing marked asymmetrical unyielded-zones in the recess corners. One comments that, under *BMP+_τ_p* and with rise in polymeric-concentration - *at low flow-rates*, plastic features are promoted (see Fig. 14b $Q \leq 5$ solutions); whilst, at *sufficiently large flow-rates*, pronounced shear-thinning is provoked, resulting in expanded fluid-response type regions (see $Q = 10$ fields).

One may gather observations at larger-Q, equivalent to intermediate deformation-rates, as the *interface between the low-Q plastic-regime and the high-Q viscoelastic-regime*. There, thixo-viscoelastic non-linearity

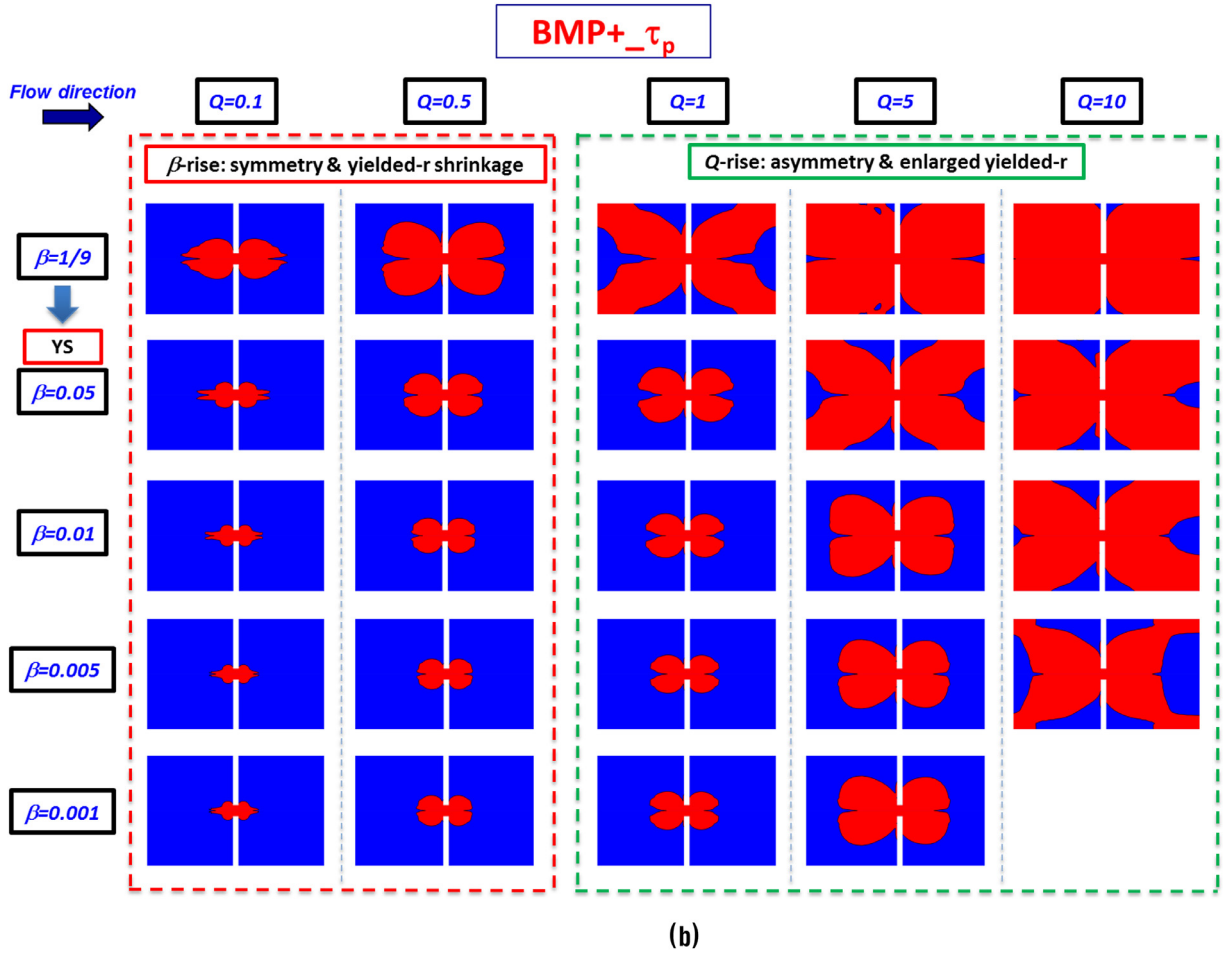

Fig. 14. Continued

is manifest, through increasing N_{1Shear}-levels and asymmetrical yield-fronts. The relatively reduced dSM asymmetry in yield-fronts at intermediate flow-rates, may be correlated with the relatively low N_{1Shear}-levels apparent under the τ_{0d}-range chosen. This is illustrated via dSM ideal-deformation solutions in Fig. 4c with $0.1 \leq N_{1Shear} \leq 20$; in contrast to the BMP+_τ_p solutions in Fig. 4f with $10^2 \leq N_{1Shear} \leq 10^4$. Moreover, at larger yield-stress levels and at intermediate shear-rates, dSM-($0.5 \leq \tau_{0d} \leq 1$) N_{1Shear}-curves decline (Fig. 4c), whilst BMP+_τ_p sustains N_{1Shear}-plateaux (Fig. 4f). As a consequence, one can devise three ways to enhance dSM nonlinear-response parametrically: (i) Q-increase (driving predictions towards a liquefied viscoelastic-response), (ii) yield-stress τ_{0d}-increase (enhancing nonlinear N_{1Shear}-response) and (iii) increase in polymer-concentration $(1-\beta)$. Nevertheless, one should bear in mind the highly non-linear dSM response, observed for example, in the dynamic yield-stress τ_{0d}-level increments demonstrated in Fig. 4c. There, at relatively low-τ_{0d}, in the range $0.02 \leq \tau_{0d} \leq 0.1$, the onset of a N_{1Shear}-plateau is apparent, and achieved with $\tau_{0d} = 1.0$. This covers the shear-rate range $0.5 \leq \lambda_1\dot{\gamma} \leq 3$ units, which is prior to the second N_{1Shear}-upturn at higher rates. Notably, for relatively high-τ_{0d} in the range $0.5 \leq \tau_{0d} \leq 1$, N_{1Shear}-maxima are recorded at $\lambda_1\dot{\gamma} \sim O(1)$; followed by N_{1Shear}-drop that extends out to shear-rates $\lambda_1\dot{\gamma} \sim O(10^2)$; prior to recovering quadratic-slope in N_{1Shear}. Hence, to amplify dSM nonlinear features in complex flow, one plausible option is to extend predictions to higher flow-rates-Q in the ($\tau_{0d} = 0.1$)-case of Fig. 4c. This case displays a rising monotonic N_{1Shear}-curve, with yield-front patterns that already display some asymmetry about the contraction-plane, see Fig. 14a ($5 \leq Q \leq 10$). One may note that analysis of thixotropic features through variation of thixotropic construction-destruction parameters on top of the viscoelastoplastic response of these models has been already explored in [6,7], in the context of viscoelastoplastic flow in rounded-corner $\alpha = 4$ circular contraction-expansion geometries. There, in accord with the findings reported in the present work, asymmetry about the contraction-plane was recorded with variation of thixotropic parameters.[1]

4.2.2. *Pressure-drops*

In Fig. 15 and under increasing yield-stress influence, total pressure-drop Δp_{total}-trends are plotted against rising flow-rate for both proposed models. This provides contrasting response across models, in terms of respective levels of pressure-drop reached. Here, dSM Δp_{total} generates a relatively tight-window of response under increasing-τ_{0d}. (Fig. 15a, fixed-β (=1/9)). This lies in stark contrast with the wide-window of response for BMP+_τ_p solutions under decreasing-β. For instance, *at fixed* $Q = 10$, the extremities of the dSM pressure-drop window lie within $\{\tau_{0d},\ \Delta p_{total}\} = \{0.02,\ 358\}$ units and $\{\tau_{0d},\ \Delta p_{total}\} = \{1,\ 512\}$ units. Comparatively, BMP+_τ_p $Q = 10$-solutions (Fig. 15b) span-out from $\{\beta,\ \Delta p_{total}\} = \{1/9,\ 400\}$ units to $\{\beta,\ \Delta p_{total}\} = \{5 \times 10^{-3},\ 5755\}$ units. Moreover, extremely polymer-concentrated BMP+_τ_p solutions ($\beta = 1 \times 10^{-3}$) can reach total pressure-drop levels as high as $\Delta p_{total} = 20{,}923$ units at $Q = 5$ (see Fig. 15b-inset). With *Q-elevation*, both dSM and BMP+_τ_p solutions display an initial sharp-rise at relatively low flow-rates, fol-

[1] Further studies on thixotropic response of viscoelastoplastic materials will appear subsequently in the current setting of α=10 sharp-cornered circular contraction-expansion flow (transient solutions) and flow past sphere (match of experiements).

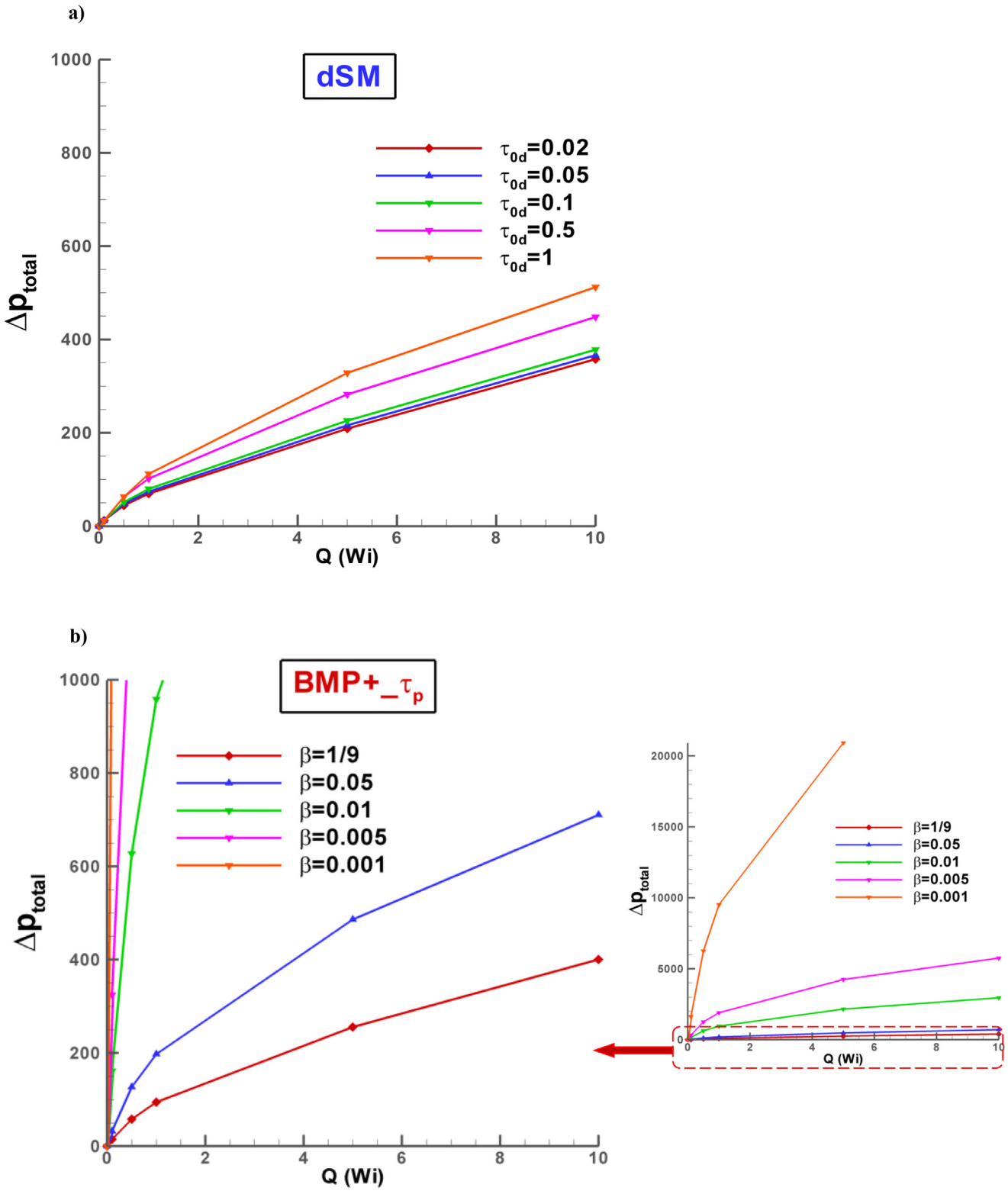

Fig. 15. Total pressure drop against Q; dSM (τ_{0d}-increase; $\beta = 1/9$) v BMP+_τ_p (β-increase); MH fluids.

lowed by a continual slope-decrease. Nevertheless, the most highly polymer-concentrated case, ($\beta = 1 \times 10^{-3}$)-BMP+_τ_p, rises rapidly with Q-increase, and barely displays slope weakening (Fig. 15b-inset). Recall, plastic-features (and hence total pressure-drop) are enhanced under dSM τ_{0d}-increase, and likewise, BMP+_τ_p performs analogously under polymer-concentration $(1-\beta)$-increase. From Fig. 4, one can gather the rheological justification for such contrasting behaviour in pressure drop. For BMP+_τ_p, polymer-concentration increase elevates first Newtonian-plateaux (*with fixing on common second plateau*), both in simple-shear and uniaxial extension. This is reflected in shear-stress T_{rz}, through rising branching patterns observed at low deformation-rates, with increase in polymer concentration. In contrast, dSM τ_{0d}-increase only af-

fects shear-stress at relatively larger deformation-rates (change noted to commence at $\lambda_1\dot{\gamma}\sim 0.3$ units). Under dSM approximation, there is unification in shear-stress at smaller shear-rates, reflected in a common first Newtonian plateau.

5. Conclusions

This study has facilitated comparative prediction for two new versions of thixotropic and viscoelastoplastic models, under circular sharp-cornered contraction-expansion flow with aspect-ratio $\alpha = 10$. Two main flow-regimes have been examined in detail under a flow-rate Q-incrementation procedure: firstly, under *viscoelastic-response*, in the high-Weissenberg setting and relatively diluted fluids; and secondly, under *plastic-response*, where predictions are explored for extremely solute-concentrated fluids and relatively low flow-rates. The viscoelastic-response regime covers the range of $(0.1 \leq Q \leq 25)$ solutions and with various polymer-concentrations $(0.1 \leq (1-\beta) \leq 8/9)$. The plastic-response regime of extremely concentrated fluids covers the range of $((1-\beta) \geq 8/9)$ in the range $(Q \leq 10)$.

In terms of the thixotropic and viscoelastoplastic *constitutive models* employed, the proposed BMP+_τ_p model possesses the complete set of features inherited from earlier variants; that is, bounded extensional-viscosity response and rising first normal-stress difference at high deformation rates. This rheology exposes an intimate and explicitly dynamic interaction between elasticity and fluid-structure. Such features are typically observed under experimental conditions in the rheology of wormlike micellar and polymeric solutions. The de Souza Mendes (dSM) model considered is the particular variant proposed in [7], coupled with the correction in the fluid-structure equation proposed by [11]. Such a time-dependent constitutive equation provides attractive normal-stress response in simple shear, with highly non-linear $N_{1\,Shear}$-trends through shear-rate rise; particularly, this dSM model variant displays a relatively narrow $N_{1\,Shear}$-plateau at moderate shear-rates, from which a second-upturn branch is gathered. Nevertheless, for greater polymer-concentration instances ($\beta = 1/9$), the dSM model may exhibit unboundedness in its extensional viscosity (dependent upon yield-stress parameters, τ_0 and τ_{0d}).

Under the *viscoelastic regime* and for highly-polymeric fluids ($\beta = 1/9$), striking correlation is observed between flow-structure derived (both in streamline and first normal-stress patterns; $0.1 \leq Q \leq 25$) and their respective intensities, with *strength of hardening* in extensional viscosity

(a) Micellar-based BMP+_τ_p: With flow-rate Q-increase, a rich flow-structure evolution is gathered. The strength of hardening drives the kinematical structures appearing and their intensity. Micellar fluids devoid of hardening (no hardening NH) evolve into symmetrical and relatively weak salient-corner flow-structures. When some extensional hardening is introduced by the variation of thixotropic parameters (moderate hardening MH-fluids), asymmetric and more intense vortices are generated. Moreover, at high deformation-rates and for NH and MH cases, there is evidence of attainment of a second Newtonian plateau, where vortex-activity retreats into the recess-corners. Finally, for strongly-hardening (SH) fluids and considering solute-concentration increase, predictions for various solvent-fractions $(1/9 \leq \beta \leq 0.9)$ reveal a complex evolution history, from salient-corner vortex activity for $\beta = 0.9$, to strong elastic-corner vortices for $\beta = 1/9$. Notably, intermediate $\beta = \{0.7, 0.8\}$ solutions display coexistence of both upstream lip- and salient-corner vortices; with greater polymer-concentration, lip-vortices tend to dominate and generate elastic-corner vortices. These are all features of challenge to experimental validation, providing benchmark predictive solutions to be reproduced by experimentalists and/or to be taken as a source of comparison by other theoretical/numerical workers.

(b) Oil-based dSM: The relatively stronger extensional response of the dSM model renders stronger kinematical activity, with larger and more active vortices that evolve directly from salient-corner vortices at low flow-rates to strong elastic-corner vortices.

Under the plastic regime, in extremely concentrated conditions $(\beta \leq 1/9)$ and low-to-moderate flow-rates $(0.1 \leq Q(Wi) \leq 10)$, with Q-rise yield-fronts reveal growing yielded-zones about the contraction-zone. These yielded-zones connect those arising in the constriction-region to those around the upstream and downstream-walls; gradually becoming asymmetrical of form with either Q-rise

(a) Under micellar BMP+_τ_p-response, plastic features are enhanced via increase in polymer-concentration $(1-\beta)$. This has a combined effect with flow-rate rise: at low flow-rates, symmetrical and reduced yielded regions are recognised; whilst Q-increase exaggerates shear-thinning (drop in viscosity levels in high-shear zones) and drives solutions towards enhanced fluidisation (high fluidity in same high-shear zones). These trends are also reflected through corresponding total pressure-drops, which rise with yield-stress increase. As such, the yield-stress enhancing-parameter plays a key role in total pressure-drop response. Under BMP+_τ_p, polymer-concentration $(1-\beta)$-increase (solvent-fraction β-decrease) provides much stronger pressure-drop adjustment than observed under dSM τ_{0d}-increase. Indeed, between these two models, two distinctly different total pressure-drop patterns can be observed.

(b) Under dSM response at fixed solvent-fraction ($\beta = 1/9$), τ_{0d}-increase generates a relatively narrow pressure-drop prediction window. In contrast, for response under BMP+_τ_p, pressure-drops span-out with polymer-concentration $(1-\beta)$-increase.

(c) Overall, BMP+_τ_p provides ultimate plateauing trends in pressure-drop at larger levels of solvent-fraction ($\beta \geq 10^{-2}$); then, these tend towards more monotonically rising forms as polymer concentration heightens still further ($\beta \leq 5\times 10^{-3}$). Such dramatic BMP+_$\tau_p$ pressure-drop elevation with solute-content (yield-stress), correlates with the rise of first Newtonian-plateaux (both in shear and extension) at low deformation-rates. In addition, the impact of shear-thinning and strain-softening become steeper. As a consequence, their effects are stark, but only when departing from the low deformation-rate regime - via Q-rise and for the more extreme polymer concentrated fluids ($\beta \leq 5\times 10^{-3}$).

Acknowledgements

Support from Consejo Nacional de Ciencia y Tecnología (CONACYT, Mexico), from UNAM (Mexico) under the projects PAIP 5000-9172 and PAPIIT IA105818, and from the Zienkiewicz Centre for Computational Engineering, Swansea University, UK, are gratefully acknowledged.

References

[1] F. Bautista, J.M. de Santos, J.E. Puig, O. Manero, Understanding thixotropic and antithixotropic behavior of viscoelastic micellar solutions and liquid crystalline dispersions. I. The model, J. Non-Newtonian Fluid Mech. 80 (1999) 93–113.
[2] O. Manero, F. Bautista, J.F.A. Soltero, J.E. Puig, Dynamics of worm-like micelles: the Cox-Merz rule, J. Non-Newtonian Fluid Mech. 106 (2002) 1–15.
[3] E.S. Boek, J.T. Padding, V.J. Anderson, P.M.J. Tardy, J.P. Crawshaw, J.R.A. Pearson, Constitutive equations for extensional flow of wormlike micelles: stability analysis of the Bautista–Manero model, J. Non-Newtonian Fluid Mech. 126 (2005) 29–46.
[4] J.E. López-Aguilar, M.F. Webster, H.R. Tamaddon-Jahromi, O. Manero, A new constitutive model for worm-like micellar systems - Numerical simulation of confined contraction-expansion flows, J. Non-Newtonian Fluid Mech. 204 (2014) 7–21.
[5] J.E. López-Aguilar, M.F. Webster, H.R. Tamaddon-Jahromi, O. Manero, High-Weissenberg predictions for micellar fluids in contraction-expansion flows, J. Non-Newtonian Fluid Mech. 222 (2015) 190–208.
[6] J.E. López-Aguilar, M.F. Webster, H.R. Tamaddon-Jahromi, O. Manero, Numerical modelling of thixotropic and viscoelastoplastic materials in complex flows, Rheol. Acta 54 (2015) 307–325.
[7] J.E. López-Aguilar, M.F. Webster, H.R. Tamaddon-Jahromi, O. Manero, A comparative numerical study of time-dependent structured fluids in complex flows, Rheol. Acta 55 (2016) 197–214.

[8] J.E. López-Aguilar, M.F. Webster, H.R. Tamaddon-Jahromi, O. Manero, Convoluted models and high-Weissenberg predictions for micellar thixotropic fluids in contraction–expansion flows, J. Non-Newtonian Fluid Mech. 232 (2016) 55–66.

[9] P.R. de Souza Mendes, Modeling the thixotropic behaviour of structured fluids, J. Non-Newtonian Fluid Mech. 164 (2009) 66–75.

[10] P.R. de Souza Mendes, Thixotropic elasto-viscoplastic model for structured fluids, Soft Matter 7 (2011) 2471–2483.

[11] P.R. de Souza Mendes, R.L. Thompson, A unified approach to model elasto-viscoplastic thixotropic yield-stress materials and apparent yield- stress fluids, Rheol. Acta 52 (2013) 673–694.

[12] M. Pérez-Camacho, J.E. López-Aguilar, F. Calderas, O. Manero, M.F. Webster, Pressure-drop and kinematics of viscoelastic flow through an axisymmetric contraction—expansion geometry with various contraction-ratios, J. Non-Newtonian Fluid Mech. 222 (2015) 260–271.

[13] J.E. López-Aguilar, M.F. Webster, H.R. Tamaddon-Jahromi, M. Pérez-Camacho, O. Manero, Contraction-ratio variation and prediction of large experimental pressure-drops in sharp-corner circular contraction-expansions–Boger fluids, J. Non-Newtonian Fluid Mech. 237 (2016) 39–53.

[14] I.A. Frigaard, K.G. Paso, P.R. de Souza Mendes, Bingham's model in the oil and gas industry, Rheol. Acta 56 (2017) 259–282.

[15] D. Bonn, J. Paredes, M.M. Denn, L. Berthier, T. Divoux, S. Manneville, Yield stress materials in soft condensed matter, Rev. Mod. Phys. 89 (2017) 035005.

[16] S. Livescu, Mathematical modelling of thixotropic drilling mud and crude oil flow in wells and pipelines-a review, J. Petrol. Sci. Eng. 98–99 (2012) 174–184.

[17] D. Fraggedakis, Y. Dimakopoulos, J. Tsamopoulos, Yielding the yield-stress analysis: a study focused on the effects of elasticity on the settling of a single spherical particle in simple yield-stress fluids, Soft Matter 12 (2016) 5378–5401.

[18] M. Dinkgreve, M.M. Denn, D. Bonn, "Everything flows?": elastic effects on startup flows of yield-stress fluids, Rheol. Acta 56 (2017) 189–194.

[19] E. Mitsoulis, J. Tsamopoulos, Numerical simulations of complex yield-stress fluid flows, Rheol. Acta 56 (2017) 231–258.

[20] R.H. Ewoldt, G.H. McKinley, Mapping thixo-elasto-visco-plastic behavior, Rheol. Acta 56 (2017) 195–210.

[21] A.Z. Nelson, R.E. Bras, J. Liu, R.H. Ewoldt, Extending yield-stress fluid paradigms, J. Rheol. 62 (2018) 357–369.

[22] A. Malkin, V. Kulichikhin, S. Ilyin, A modern look on yield stress fluids, Rheol. Acta 56 (2017) 177-15.

[23] P. Saramito, A. Wachs, Progress in numerical simulation of yield stress fluid flows, Rheol. Acta 56 (2017) 211–230.

[24] J. Yang, Viscoelastic wormlike micelles and their applications, Curr. Opin. Colloid Interface Sci. 7 (2002) 276–281.

[25] C.A. Dreiss, Wormlike micelles: where do we stand? Recent developments, linear rheology and scattering techniques, Soft Matter 3 (2007) 956–970.

[26] C. Van Der Geest, V.C. Bizotto-Guersoni, D. Merino-Garcia, A.C. Bannwart, A unified approach to model elasto-viscoplastic thixotropic yield-stress materials and apparent yield- stress fluids, Rheol. Acta 54 (2015) 545–561.

[27] C.J. Dimitriou, G.H. McKinley, A comprehensive constitutive law for waxy crude oil: a thixotropic yield stress fluid, Soft Matter 10 (2014) 6619–6644.

[28] P. Saramito, A new constitutive equation for elastoviscoplastic fluid flows, J. Non-Newtonian Fluid Mech. 145 (2007) 1–14.

[29] P. Saramito, A new elastoviscoplastic model based on the Herschel–Bulkley viscoplastic model, J. Non-Newtonian Fluid Mech. 158 (2009) 154–161.

[30] P. Sollich, Rheological constitutive equation for a model of soft glassy materials, Phys. Rev. E 58 (1998) 738–759.

[31] P. Sollich, F. Lequeux, P. Hébraud, M.E. Cates, Rheology of soft glassy materials, Phys. Rev. Lett. 78 (1997) 2020–2023.

[32] R. Radhakrishnan, T. Divoux, S. Manneville, S.M. Fielding, Understanding rheological hysteresis in soft glassy materials, Soft Matter 13 (2017) 1834–1852.

[33] R. Radhakrishnan, S.M. Fielding, Shear banding of soft glassy materials in large amplitude oscillatory shear, Phys. Rev. Lett. 117 (2016) 188001.

[34] L. Bocquet, A. Colin, A. Ajdari, Kinetic theory of plastic flow in soft glassy materials, Phys. Rev. Lett. 103 (2009) 036001.

[35] M.L. Falk, J.S. Langer, Dynamics of viscoplastic deformation in amorphous solids, Phys. Rev. E 57 (1998) 7192–7205.

[36] F. Bautista, J.F.A. Soltero, J.H. Pérez-López, J.E. Puig, O. Manero, On the shear banding flow of elongated micellar solutions, J. Non-Newtonian Fluid Mech. 94 (2000) 57–66.

[37] J.P. García-Sandoval, O. Manero, F. Bautista, J.E. Puig, Inhomogeneous flows and shear-banding formation in micellar solutions: predictions of the BMP model, J. Non-Newtonian Fluid Mech. 179–180 (2012) 43–54.

[38] J.E. López-Aguilar, M.F. Webster, H.R. Tamaddon-Jahromi, O. Manero, Shear-banding predictions for wormlike micellar systems under complex flow, J. Non-Newtonian Fluid Mech. (2018) *Under review*.

[39] J.E. López-Aguilar, H.R. Tamaddon-Jahromi, M.F. Webster, K. Walters, Numerical vs experimental pressure drops for Boger fluids in sharp-corner contraction flow, Phys. Fluids 28 (2016) 103104.

[40] J.E. López-Aguilar, M.F. Webster, H.R. Tamaddon-Jahromi, O. Manero, D.M. Binding, K. Walters, On the use of continuous spectrum and discrete-mode differential models to predict contraction-flow pressure drops for Boger fluids, Phys. Fluids 29 (2017) 121613.

[41] H.R. Tamaddon-Jahromi, J.E. López-Aguilar, M.F. Webster, On modelling viscoelastic flow through abrupt circular 8:1 contractions – matching experimental pressure–drops and vortex structures, J. Non-Newtonian Fluid Mech. 251 (2017) 28–42.

[42] M. Nyström, H.R. Tamaddon-Jahromi, M. Stading, M.F. Webster, Numerical simulations of Boger fluids through different contraction configurations for the development of a measuring system for extensional viscosity, Rheol. Acta 51 (2016) 713–727.

[43] M. Nyström, H.R. Tamaddon-Jahromi, M. Stading, M.F. Webster, Extracting extensional properties through excess pressure drop estimation in axisymmetric contraction and expansion flows for constant shear viscosity, extension strain-hardening fluids, Rheol. Acta 55 (2016) 373–396.

[44] M. Nyström, H.R. Tamaddon-Jahromi, M. Stading, M.F. Webster, Hyperbolic contraction measuring systems for extensional flow, Mech. Time-Dependant Mater. 21 (2017) 455–479.

[45] H.A. Barnes, The yield stress – a review or '$\pi\alpha\nu\tau\alpha\ \rho$ϵι' – everything flows? J. Non-Newtonian Fluid Mech. 81 (1999) 133–178.

[46] H.A. Barnes, The 'yield stress myth?' paper – 21 years on, Appl. Rheol. 17 (2007) 43110-1-43110-5.

[47] H. Matallah, P. Townsend, M.F. Webster, Recovery and stress-splitting schemes for viscoelastic flows, J. Non-Newtonian Fluid Mech. 75 (1998) 139–166.

[48] P. Wapperom, M.F. Webster, A second-order hybrid finite-element/volume method for viscoelastic flows, J. Non-Newtonian Fluid Mech. 79 (1998) 405–431.

[49] M.F. Webster, H.R. Tamaddon-Jahromi, M. Aboubacar, Time-dependent algorithms for viscoelastic flow: finite element/volume schemes, Numer. Methods Partial Differ. Equations 21 (2005) 272–296.

[50] F. Belblidia, H. Matallah, M.F. Webster, Alternative subcell discretisations for viscoelastic flow: velocity-gradient approximation, J. Non-Newtonian Fluid Mech. 151 (2008) 69–88.

[51] J.P. Rothstein, G.H. McKinley, The axisymmetric contraction-expansion: the role of extensional rheology on vortex growth dynamics and the enhanced pressure drop, J. Non-Newtonian Fluid Mech. 98 (2001) 33–63.